minerals

MDPI

Article

CO_2 Absorption and Magnesium Carbonate Precipitation in $MgCl_2$–NH_3–NH_4Cl Solutions: Implications for Carbon Capture and Storage

Chen Zhu [1], Han Wang [1], Gen Li [2], Siyu An [1], Xiaofeng Ding [1], Hui Henry Teng [1,3] and Liang Zhao [1,*]

[1] School of Earth Sciences and Engineering, Nanjing University, Nanjing 210046, China; zhuchen.nju@gmail.com (C.Z.); wanghan@smail.nju.edu.cn (H.W.); ansiyunju@gmail.com (S.A.); dingxiaofeng.nju@gmail.com (X.D.); hteng@gwu.edu (H.H.T.)

[2] Department of Earth Sciences, University of Southern California, Los Angeles, CA 90089, USA; genli@usc.edu

[3] Department of Chemistry, The George Washington University, Washington, DC 20052, USA

* Correspondence: zhaoliang@nju.edu.cn; Tel.: +86-25-8968-0830

Received: 23 August 2017; Accepted: 11 September 2017; Published: 19 September 2017

Abstract: CO_2 absorption and carbonate precipitation are the two core processes controlling the reaction rate and path of CO_2 mineral sequestration. Whereas previous studies have focused on testing reactive crystallization and precipitation kinetics, much less attention has been paid to absorption, the key process determining the removal efficiency of CO_2. In this study, adopting a novel wetted wall column reactor, we systematically explore the rates and mechanisms of carbon transformation from CO_2 gas to carbonates in $MgCl_2$–NH_3–NH_4Cl solutions. We find that reactive diffusion in liquid film of the wetted wall column is the rate-limiting step of CO_2 absorption when proceeding chiefly through interactions between CO_2(aq) and NH_3(aq). We further quantified the reaction kinetic constant of the CO_2–NH_3 reaction. Our results indicate that higher initial concentration of NH_4Cl ($\geq$ 2 mol·L^{-1}) leads to the precipitation of roguinite [$(NH_4)_2Mg(CO_3)_2 \cdot 4H_2O$], while nesquehonite appears to be the dominant Mg-carbonate without NH_4Cl addition. We also noticed dypingite formation via phase transformation in hot water. This study provides new insight into the reaction kinetics of CO_2 mineral carbonation that indicates the potential of this technique for future application to industrial-scale CO_2 sequestration.

Keywords: absorption rate; carbon dioxide; carbon capture and storage; magnesium carbonate

1. Introduction

1.1. CO_2 Mineral Sequestration

Among the currently recognized strategies for Carbon Capture and Storage (CCS), sequestering atmospheric CO_2 in mineral forms, as first introduced by Seifritz [1], is the only known approach to permanent CO_2 storage. Mineral carbon sequestration mainly uses naturally abundant material resources like Mg-silicates [2,3] to react with atmospheric CO_2 to form carbonate minerals. Compared to other options (e.g., storing CO_2 in geological reservoirs like bedrock), mineral carbon sequestration has two major advantages: nearly unlimited raw material supplement, and relatively longer-term storage (>1 Myr, over geological timescales) [4]. However, at the Earth's surface conditions, the rate of the silicate-CO_2 reaction, or carbonation, is quite low (~10^{-10} to 10^{-17} mol·m^{-2}·s^{-1}) [5]. To accelerate the reaction rate, several strategies have been tested, including increasing the ambient temperature and CO_2 pressure, enhancing the reactive surface areas of silicates [6–8], and removing the passivating layer on minerals [2,3,9,10]. Although those procedures show promise, they are often energy-intensive, making the carbonation process expensive and less practical [11].

The last decades have seen significant advances in the development of techniques aiming at economic and energy-efficient mineral carbon sequestration. Many groups have made efforts to accelerate silicate-CO_2 reaction rates. Notably, a pH-swing reaction path, which separated divalent ion leaching and carbonation process, was developed and proven to effectively enhance the mineral dissolution rate and optimize carbonate precipitation [12,13]. Extensive studies have focused on the mineral dissolution process. Among the many materials tested, magnesium-rich materials are thought to be good candidates for carbonation due to their natural abundance [14] and relatively higher unit mass binding efficiency (e.g., as compared to calcium). For example, physical activation (grinding [15–17] or heating [18,19]), chemical leaching (acid [20–22], recyclable ammonium salt [23,24] or non-acidic ionic solutions [25]), bioleaching [26,27] were applied to Mg rich minerals to dissolve and concentrate Mg. However, the other CO_2 absorption and carbonate precipitation steps have been less explored. Only a few studies have focused on testing the reactive absorption and precipitation using materials extracted from natural minerals. Soluble barium salt was used to absorb CO_2 via reactive crystallization [28–30], but was limited by the low natural abundance and toxicity. $Ca(OH)_2$ was also a possible absorbent [31,32], but $Ca(OH)_2$ solid is usually produced from $CaCO_3$ with CO_2 as a byproduct, negating its sequestering function. Reactive absorption of CO_2 in alkaline $MgCl_2$ solutions [33] or $Mg(OH)_2$ slurries successfully precipitated nesquehonite ($MgCO_3{\cdot}3H_2O$), a common mineral, at Earth's surface conditions [34,35]. Yet, the reaction kinetics of CO_2 absorption and carbonate precipitation in Mg solutions remains insufficiently understood. Specifically, few studies have investigated the CO_2 mass transfer processes on the gas-liquid interface, or how precipitated minerals vary under elevated ammonium nitrogen concentrations apart from temperature, duration, and Mg/Ca ratio [36–38].

To fill the knowledge gap, we systematically investigated the reaction kinetics and mass transfer process in CO_2–$MgCl_2$–NH_3–NH_4Cl solutions, as a case study to understand CO_2 absorption and precipitation in Mg solutions. Our work combined theoretical modeling of solution chemistry and laboratory experiments. We carefully designed and optimized the solution recipes via geochemical modeling. We built a novel wetted wall column device and conducted a series of controlled experiments of CO_2 absorption and precipitation. We calculated reaction kinetic parameters and discussed the potential controlling factors. We studied how the precipitation products change under different conditions, and developed original methods to obtain industrially useful Mg carbonates. Our work contributes to a better understanding of the CO_2 absorption and precipitation processes in industrially practical systems (e.g., CO_2–Mg solutions), and provides valuable information for the design of absorption devices and optimizing absorbent composition.

1.2. Chemistry and Kinetics of the CO_2–$MgCl_2$–NH_3–NH_4Cl System

A brief introduction to the aqueous phase reactions after gaseous CO_2 diffusing into the solution, together with the associated kinetic equations, is given below. After entering the aqueous phase, CO_2 reacts with water, hydroxide ions, and ammonia simultaneously [39–41]. This process can be expressed by the following chemical reactions:

$$CO_2(aq) + H_2O \leftrightarrow HCO_3^- + H^+ \tag{1}$$

$$CO_2(aq) + OH^- \leftrightarrow HCO_3^- \tag{2}$$

$$CO_2(aq) + 2NH_3(aq) \leftrightarrow NH_2COO^- + NH_4^+ \tag{3}$$

Equation (1) combines the hydration of CO_2 with rapid dissociation to HCO_3^- and H^+, and its reaction rate can be written as:

$$r_{CO_2-H_2O} = k'_{H_2O} C_{CO_2} \tag{4}$$

where $r_{CO_2-H_2O}$ is the rate of reactions between CO_2 and water, k'_{H_2O} is the rate constant, and C_{CO_2} represent the concentration of CO_2. The temperature (T, in Kelvin) dependence of rate constant (k_{H_2O}, in s^{-1}) has been determined previously [42] as:

$$\log\left(k'_{H_2O}\right) = 329.850 - 110.541\log(T) - (17{,}265.4/T) \tag{5}$$

Under experimental conditions (T = 298.15 K), k'_{H_2O} is 0.026 s^{-1}. Similarly, the reaction rate constant of Equation (2), given in $m^3{\cdot}mol^{-1}{\cdot}s^{-1}$, is

$$\log\left(k_{OH^-}\right) = 10.635 - (2895/T) \tag{6}$$

which is 8.41 $m^3{\cdot}mol^{-1}{\cdot}s^{-1}$ at 298.15 K [42].

For the reaction (Equation (3)) between $CO_2(aq)$ and $NH_3(aq)$, a multi-step zwitterion mechanism is often used [40]: A CO_2 molecule reacts with an ammonia molecule to form a zwitterion, then gets deprotonated by bases (e.g., NH_3, OH^-, and H_2O) in solution to form carbamate. For the carbamate, a hydrolytic reaction may occur to convert carbamate to bicarbonate. The detailed reaction paths of Equation (3) are:

$$CO_2(aq) + NH_3 \overset{k_2/k_{-1}}{\leftrightarrow} {}^{\oplus}NH_3COO^{\ominus} \tag{7}$$

$$ {}^{\oplus}NH_3COO^{\ominus} + \text{Base} \overset{k_b}{\leftrightarrow} NH_2COO^- + \text{BaseH}^+ \tag{8}$$

$$NH_2COO^- + H_2O \leftrightarrow NH_3 + HCO_3^-. \tag{9}$$

Combining Equations (3) and (7)–(9), the rate expression for Equation (3) can be obtained as:

$$r_{CO_2-NH_3} = \frac{C_{CO_2}C_{NH_3}}{\left(\frac{1}{k_2}\right) + \left(\frac{k_{-1}}{k_2}\right)\left(\frac{1}{\sum b k_b C_B}\right)}, \tag{10}$$

where b represents any base in the solution and C_B is their concentrations. k_2 and k_{-1} are the forward and backward rate constant of Equation (7), respectively. In this case, a base can be a water molecule, hydroxide ions, or ammonia. Replacing the base using the specific molecules, Equation (10) can be rewritten as:

$$r_{CO_2-NH_3} = \frac{C_{CO_2}C_{NH_3}}{\left(\frac{1}{k_2}\right) + \left(\frac{k_{-1}}{k_2}\right)\left(\frac{1}{\sum k_{b,H_2O}C_{H_2O} + k_{b,\,OH^-}k_{OH^-} + k_{b,NH_3}C_{NH_3}}\right)} \tag{11}$$

Note that in this work, ammonia is introduced as a base to bind hydrogen ions and buffer pH change.

$$NH_3 + H^+ \leftrightarrow NH_4^+ \tag{12}$$

The bicarbonate resultant from Equations (1), (2), and (9) transforms into carbonate and carbonic acid through

$$HCO_3^- \leftrightarrow CO_3^{2-} + H^+ \tag{13}$$

$$HCO_3^- + H^+ \leftrightarrow H_2CO_3 \tag{14}$$

When Mg^{2+} is present, various forms of magnesium carbonates can precipitate from saturated solution [43–45]. The anhydrous form of Mg-carbonate, magnesite ($MgCO_3$), is usually difficult to precipitate under ambient conditions, but relatively easier under elevated CO_2 pressure and temperature (>90 °C), likely caused by the high hydration energy of Mg^{2+} ions in aqueous solution [46]. A highly hydrated Mg-carbonate, lansfordite ($MgCO_3{\cdot}5H_2O$), appears near the freezing point of water (4~9 °C). Other hydrated Mg-carbonates, such as nesquehonite ($MgCO_3{\cdot}3H_2O$), hydromagnesite ($Mg_5(CO_3)_4(OH)_2{\cdot}4H_2O$), and dypingite ($Mg_5(CO_3)_4(OH)_2{\cdot}5H_2O$), can form within wider ranges of temperature and pressure. Nesquehonite is a common magnesium carbonate precipitated under experimental conditions at room temperature and CO_2 pressure due to its kinetic advancement [47]. However, the natural occurrence of nesquehonite in large deposition is rather rare compared with other magnesium carbonates, such as hydromagnesite [48], magnesite [49,50], etc. Fresh nesquehonite can be seen under low temperature in a natural environment (e.g., [51–53]). Although it is not abundant, field and experimental evidence shows that nesquehonite could act as a precursor of more abundant hydromagnesite or magnesite [43,50,54], and dypingite is a transitory phase during this transformation [36,55]. Temperature, fluid pH, and CO_2 partial pressure are important parameters of phase transformation [55,56]. A generalized reaction equation representing the precipitation of these Mg-carbonates can be written as:

$$(x + y)\mathrm{Mg}^{2+} + x\mathrm{CO}_3^{2-} + 2y\mathrm{OH}^- + z\mathrm{H_2O} \leftrightarrow x\mathrm{MgCO}_3 \cdot y\mathrm{Mg(OH)}_2 \cdot z\mathrm{H_2O(s)}. \quad (15)$$

In solutions with more complex compositions, magnesium can form a crystalline double carbonate with the alkali metals in the form of $R_2CO_3 \cdot MgCO_3 \cdot 4H_2O$, where R represents K^+, Rb^+, Cs^+, and NH_4^+.

2. Materials and Methods

2.1. Reagents

We chose magnesium chloride hexahydrate ($MgCl_2 \cdot 6H_2O$) as the magnesium source material, and ammonia as the base to adjust the solution pH. Analytical graded aqueous NH_3 solution (28 wt %, produced by Nanjing Chemical Reagent Co., Ltd., Nanjing, China), was used to adjust the solution pH. Distilled deionized water produced by a High-tech^{TM} ultra-pure water system (resistivity >18.0 MΩ·cm) was used to wash any precipitated solid product and to dissolve analytical graded $MgCl_2 \cdot 6H_2O$ and NH_4Cl solids (produced by Nanjing Chemical Reagent Co., Ltd.) to make the desired solutions. Diluted HCl (0.1 $mol \cdot L^{-1}$) solution was also used to clean the liquid system after each run. The CO_2-N_2 mixture with a specified CO_2 concentration was made by mixing pure (>99.99%) CO_2 and N_2 from gas cylinders, with their proportions regulated by flow rate controllers.

2.2. Absorption Experiments

To investigate CO_2 absorption and Mg-carbonate precipitation kinetics in detail, we adopted a wetted wall column device that was originally designed for gas-liquid reaction, and updated the device to make it suitable for the study of triple phase reaction kinetics (Figure 1). A detailed description and the testing results of the device are reported in Zhu et al. (2016) [57]. We briefly introduce the key components and functions here. The core of the column (Figure 1a) was made of a hollow stainless tube, allowing homogeneous distribution of liquid film on its outer surface, forming a uniform gas-liquid contact layer with a film thickness of 0.29 mm and a total area (a) of 3364 mm^2. The mole amount of CO_2 aborted within a certain time interval (~1 s) was calculated by measuring the difference of CO_2 flux between gas inlet (n_i^{in}) and outlet (n_i^{out}) based on the ideal gas law ($PV = nRT$). A crystallizer was attached to the wetted wall column, allowing precipitation of solids and solution sampling, while solution pH was kept constant by a proportional integral (PI) control sequence managing NH_3 addition. The pH in both the wetted wall column and the crystallizer was kept constant by circulating the solution through two peristaltic pumps (E in Figure 1b).

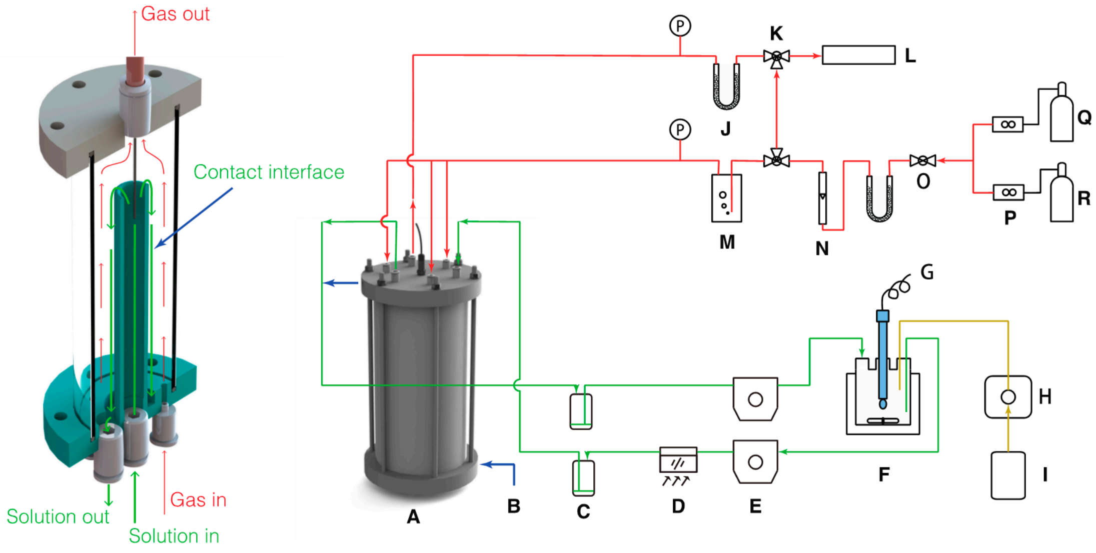

(a) (b)

Figure 1. Schemes of the experimental setup for CO_2 absorption and Mg-carbonate precipitation kinetic study: (**a**) Core of the modified wetted-wall column (part A), achieving gas absorption into solution through a measurable contact layer; (**b**) parts that constitute the whole experimental system (A: wetted-wall column; B: circulating water; C: damper; D: spectrophotometer; E: peristaltic pump; F: jacket reactor; G: pH electrode with temperature sensor; H: high-performance liquid chromatography (HPLC) pump; I: reactant tank; J: dehydration; K: three-way valve; L: gas analyzer; M: saturator; N: rotameter; O: needle valve; P: mass flow meter; Q: CO_2 cylinder; R: N_2 cylinder).

A normal experimental run starts with purging the reaction chamber with N_2 and rinsing the liquid tubing using deionized water and the reaction solution. Subsequently, the peristaltic pumps were started up after filling the glass reactor with 660 mL of the reaction solution. Formation of homogenous liquid film was confirmed by a visual check. Next, the reaction chamber was bypassed and CO_2 was introduced into the gas line. The volumetric fraction of CO_2 was determined by a non-dispersive infrared (NDIR) gas analyzer (15.0% for all experiments). Once the solution reached set temperature, the CO_2–N_2 mixture was fed into the reaction chamber, and the pH control sequence was launched. Real-time experimental status was monitored and recorded, including all parameters of interests such as room temperature, solution pH, solution temperature, base adding rate, solution transmittance, reaction chamber temperature, and the CO_2 volumetric fraction at the gas outlet. An individual experiment runs end when the solution transmittance reaches a stable reading. Afterwards, diluted hydrochloric acid was used to wash the entire liquid line and the reaction chamber, to eliminate potential crystal seed contamination. Solution samples from experiments C, E, F, and G (Table 1) were collected and filtered at certain time intervals (20–30 min). The filtrate was acidized immediately to avoid nitrogen loss due to vaporization. Total ammonium nitrogen was measured using the distillation and titration method. The total carbon (TC, in mole) absorbed into the solution was calculated using the equation below:

$$\mathrm{TC}(t) = \sum_{0}^{i=t}\left(n_i^{in} - n_i^{out}\right) \tag{16}$$

where t is the sampling time, and n_i^{in} and n_i^{out} represent the amount of CO_2 absorbed (mol) during the time interval (~1 s) in and out of the wetted wall column, respectively. Thus, the experimental absorption rate (φ_{CO_2}) is defined as

$$\varphi_{CO_2} = \frac{\mathrm{TC}(t_2) - \mathrm{TC}(t_1)}{(t_2 - t_1)a} \tag{17}$$

Table 1. Chemistry of starting solutions for CO_2 absorption and Mg-carbonate precipitation experiments. Reaction temperature was kept at 25 °C.

ID	Base	pH [1]	C^0_{Mg} [2] mol·L^{-1}	$C^0_{NH_4Cl}$ mol·L^{-1}	Duration s	Mg-Carbonate Phase [3]	t_{ind} [4] s
A	NH_3	9.00	0.00	0.0	16,532	N/A	-
B	NH_3	9.00	0.05	0.0	22,728	Nes	12,792
C	NH_3	9.00	0.10	0.0	19,117	Nes	9302
D	NH_3	9.00	0.20	0.0	22,416	Nes	7899
E	NH_3	8.76	0.10	0.0	20,000	Nes	11,222
F	NH_3	9.16	0.10	0.0	18,380	Nes	8036
G	NH_3	9.74	0.10	0.0	18,839	Nes	4185
H	NH_3	9.20	0.20	2.0	28,800	Nes + Rog	-
I	NH_3	9.63	0.20	6.7	19,740	Rog	-
X	NaOH	9.00	0.00	0.0	16,353	N/A	-

[1] pH indicates the solution pH value maintained by the pH controller; [2] C^0_{Mg} and $C^0_{NH_4Cl}$ represent initial Mg and NH_4Cl concentrations; [3] "Nes" and "Rog" represent nesquehonite and roguinite $[(NH_4)_2Mg(CO_3)_2{\cdot}4H_2O]$ respectively; [4] t_{ind} represents the time lag of nesquehonite precipitation.

Note that for experiments H and I, a uniform liquid film is difficult to maintain, thus the CO_2 absorption rate data of these experiments are unavailable. A pre-established CO_2 absorption baseline, which uses NaOH solution (pH = 9.00, 25 °C, experiment X) as the absorbent [57], was adopted to run parallel experiments for comparison to the previous experiments run in NH_3 solutions, for the purpose of revealing the role of NH_3 in absorption.

2.3. Mg-Carbonate Precipitation and Phase Transformation Experiments

The solid products produced after each absorption experiment were filtered and air-dried, followed by X-ray powder diffraction (XRD) characterization (Rigaku, DMX-IIIA, Tokyo, Japan). Mg concentration in the solution sample from experiment C was analyzed by an inductively coupled plasma atomic emission spectrometer (ICP-AES, Thermo Scientific, iCAP 6000, Waltham, MA, USA). The amount of Mg precipitated was then calculated by subtracting the remaining Mg in solution from the total initial Mg in system. If the precipitated Mg-carbonate was nesquehonite, the amount of carbon (mol) removed from the solution was determined as equivalent to the amount of precipitated Mg, and the dissolved inorganic carbon (DIC) was calculated by subtracting the precipitated carbon from the TC absorbed. The obtained data were then used to estimate the saturation state of nesquehonite.

If non-nesquehonite Mg-carbonate was precipitated (e.g., roguinite in this study), solid phase transformation experiments were then conducted to obtain nesquehonite or more stable basic magnesium carbonate hydrate due to their diverse industrial applications. Specifically, 5 g of air-dried solid product from experiment I (Table 1) were placed in a 100 mL flask and further washed using 50 mL distilled deionized water. The slurry was then set in a water bath and stirred for 1 h under various temperature settings (20 °C, 50 °C, and 80 °C). After washing, the mixture was filtered and characterized using XRD.

2.4. Theoretical Modeling of Solution Chemistry

Our previous studies concerning nesquehonite nucleation [58,59] demonstrated the importance of precise control of solution chemistry in avoiding $Mg(OH)_2$ precipitation (e.g., brucite). In the present work, we constrained solution chemistry based upon the results of equilibrium modeling. Assuming fast ionic reactions, sauturation index (SI, the logarithm of saturation degree ($\Omega = IAP/K_{sp}$) to the base 10, where IAP and K_{sp} represent the ionic activity product and solubility product respectively) of both nesquehonite and brucite under various total carbon and ammonium nitrogen concentration were calculated using the PHREEQC program (a computer program for aqueous geochemical calculations). pH was allowed to drift, while Mg concentration was set at 0.10 mol·L^{-1} during modeling. Such equilibrium treatment of bulk solution chemistry would introduce ~8% uncertainty according to our previous test [57]. To avoid the formation of brucite, a common co-product at high pH, and to form pure nesquehonite, the solution should be supersaturated with respect to nesquehonite and unsaturated to brucite. During CO_2 absorption, ammonia was added to adjust pH, because the solution pH was also a key factor determining precipitated minerals and would decrease with the accumulation of carbon species. As shown in Figure 2 (shaded area), once the concentrations of ammonia and carbon are carefully controlled at any given Mg concentration, pure nesquehonite can be obtained with no precipitation of brucite. Such a state can be maintained throughout the whole process of CO_2 absorption and Mg-carbonate precipitation. For reference, Table 2 shows the equilibrium constants of several reactions and their sources. For the other Mg-carbonate, roguinite, thermodynamic data are unavailable.

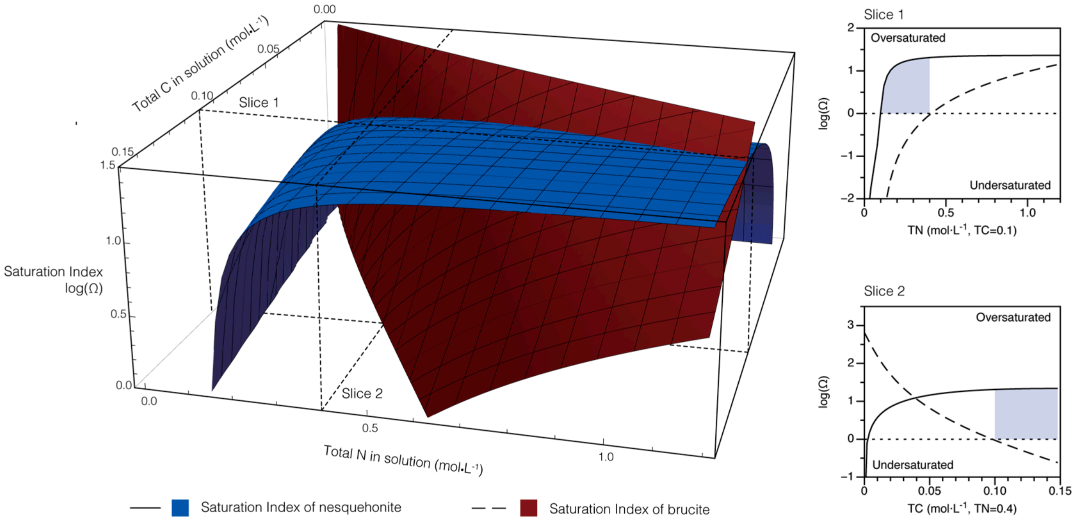

Figure 2. Saturation index SI, logΩ of nesquehonite and brucite versus concentrations of TC and TN. The 3D surface graph on the left shows that with careful chosen of solution composition, nesquehonite can be kept oversaturated (SI > 0) while brucite can be kept undersaturated (SI < 0). The 2D lines on the right (slice 1 and slice 2) indicate the preferred solution chemistry (shaded area) to produce pure nesquehonite at constant TC (0.1 $mol \cdot L^{-1}$, slice 1) or TN (0.4 $mol \cdot L^{-1}$, slice 2). Mg concentration is set as 0.10 $mol \cdot L^{-1}$, and temperature is 25 °C.

Table 2. Equilibrium constants of various ionic reactions in bulk solution at 25 °C and their sources.

Equation	pK [1]	Source
(1)	5.86	[60]
(2)	−8.03	Calculated [2]
(3)	−3.29	[61,62]
(12)	−9.24	[63]
(13)	10.32	[64]
(14)	−6.37	[64]
(15)	−5.34	[65–69] [3]

[1] pK is defined as –log(K); [2] Calculated from the equilibrium constants of Equation (1) and pure water (pKw = 14); [3] Average value of nesquehonite solubility product in the literature.

3. Results

In this section, we report our results from the experiments of CO_2 absorption under various initial Mg concentrations and pH values, and of Mg-carbonate precipitation under different ammonium concentrations.

3.1. CO_2 Absorption under Changing Mg Initial Concentration

Figure 3a shows how the total carbon absorbed (TC) evolves over time under variable initial Mg concentrations from 0.00 to 0.20 mol·L^{-1}. The overall trends of TC evolution with time are similar despite the varying Mg concentrations. The averaged initial absorption rate (for the first two minutes of absorption, Figure 3b) of those experiments is 8.38(74) × 10^{-4} mol·m^{-2}·s^{-1}, close to that of NaOH absorption baseline (experiment X, 7.70 × 10^{-4} mol·m^{-2}·s^{-1}). The instantaneous CO_2 absorption rate increases over time in the NH_3 system but not in the NaOH system. The averaged final absorption rate (in a span of four hours) between experiment A–E is 1.28(4) × 10^{-3} mol·m^{-2}·s^{-1}, which is almost double that of experiment X (also 7.70 × 10^{-4} mol·m^{-2}·s^{-1}). The increased CO_2 absorption rates over time indicate kinetic accelerations of the CO_2–NH_3–$MgCl_2$ system. The normalized deviations in both initial and final absorption rates over experiments A–E, 8.8% and 3.5%, respectively, are insignificant, suggesting that changing initial Mg concentration has a limited effect on the CO_2 absorption. The initial Mg concentration does seem to affect the timing of nesquehonite's first occurrence. As shown in Table 1, no Mg-carbonate appears when Mg concentration is zero, and a higher initial Mg concentration shortens the time lag of nesquehonite precipitation (from 3.6 h at 0.05 mol·L^{-1} to 2.2 h at 0.2 mol·L^{-1}). Another interesting observation is that experiments A–E all have similar, smooth, and continuous TC-time curves, suggesting that precipitation does not seem to lead to abrupt change in the absorption process.

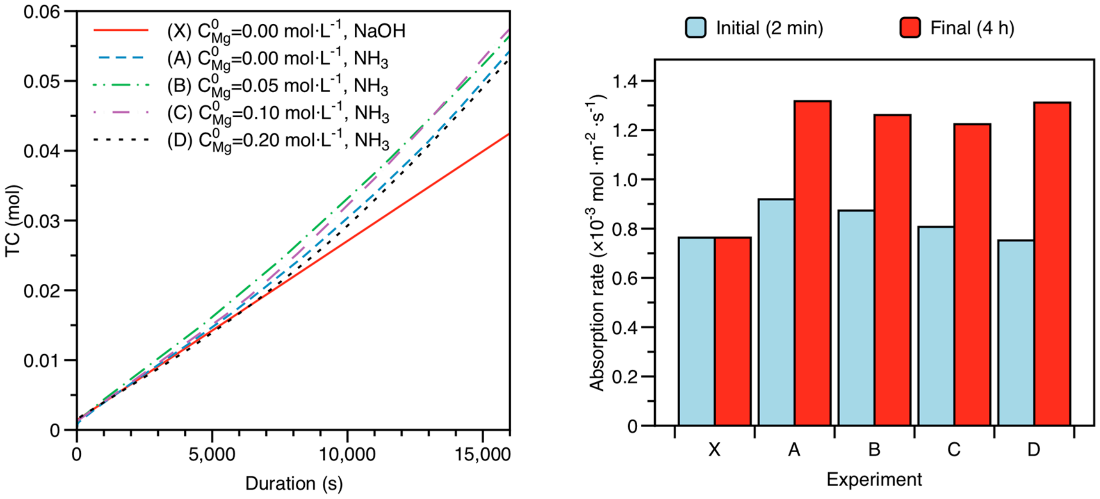

(a) (b)

Figure 3. CO_2 absorption data of several experiments with various initial Mg concentration C^0_{Mg} but same pH (9.00): (**a**) Amount of carbon absorbed against experiment duration; (**b**) CO_2 absorption rate (φ_{CO_2}) at the beginning (averaged over the initial two minutes) and near the end (averaged over four hours, the full duration of the experiment).

3.2. CO_2 Absorption under Changing Solution pH

Figure 4a shows the TC-time curves for experiments C, E, F and G under the same initial Mg concentration (C^0_{Mg} = 0.10 mol·L^{-1}) but different pH values (from 8.76 to 9.74). Different from Figure 3a, the TC-time curves in Figure 4a separate from each other more significantly, pointing to a stronger pH effect on CO_2 absorption kinetics.

Although these experiments share similar initial CO_2 absorption rates (averaged over the first two minutes ~8(1) × 10^{-4} mol·m^{-2}·s^{-1}, Figure 4b), those with higher pH lead to a faster four hour-averaged absorption rate (0.97 to 3.76 × 10^{-3} mol·m^{-2}·s^{-1}). The delay for nesquehonite precipitation also shortens with increasing pH, from 3.1 h at pH 8.76 to 1.2 h at pH 9.74 (Table 1).

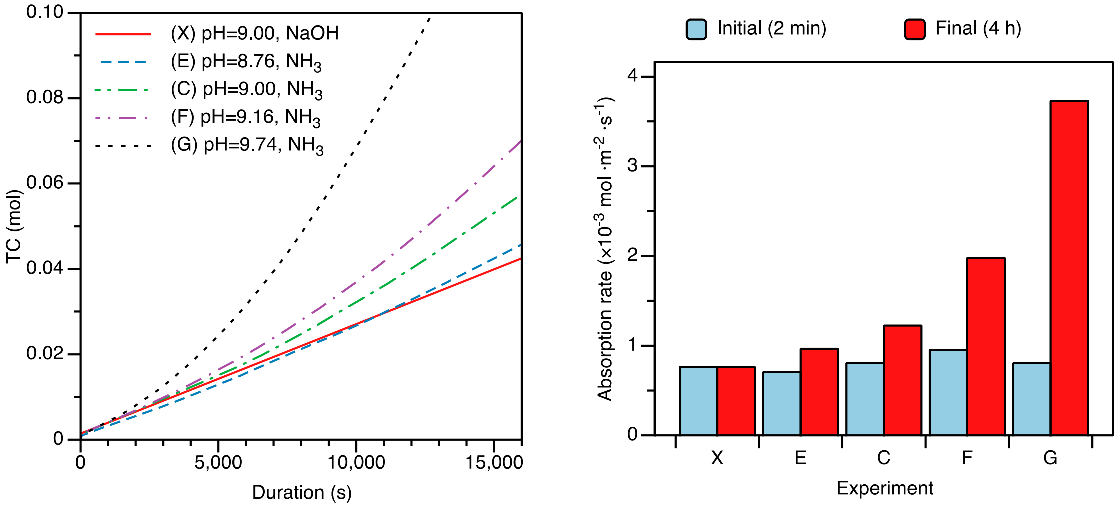

(a) (b)

Figure 4. CO_2 absorption data of several experiments with various solution pH but same C^0_{Mg} (0.10 mol·L^{-1}): (**a**) Amount of carbon absorbed against experiment duration; (**b**) CO_2 absorption rate (φ_{CO_2}) at the beginning and near the end. Initial and final rates of the same experiment are placed side by side.

3.3. Mg-Carbonate Precipitated under Changing Ammonium Concentration and Its Purification

In solutions without initial NH_4Cl addition (experiments A–G), nesquehonite is the main precipitate, as revealed by XRD (Figure 5 and Table 1). However, with higher initial NH_4Cl concentration (>2 mol·L^{-1}), roguinite starts to form (Figure 5a). Pure roguinite appeared when initial NH_4Cl reached 6.7 mol L^{-1}, but transformed to nesquehonite at 20–50 °C (Figure 5b) and dypingite at 80 °C when washing at such a temperature.

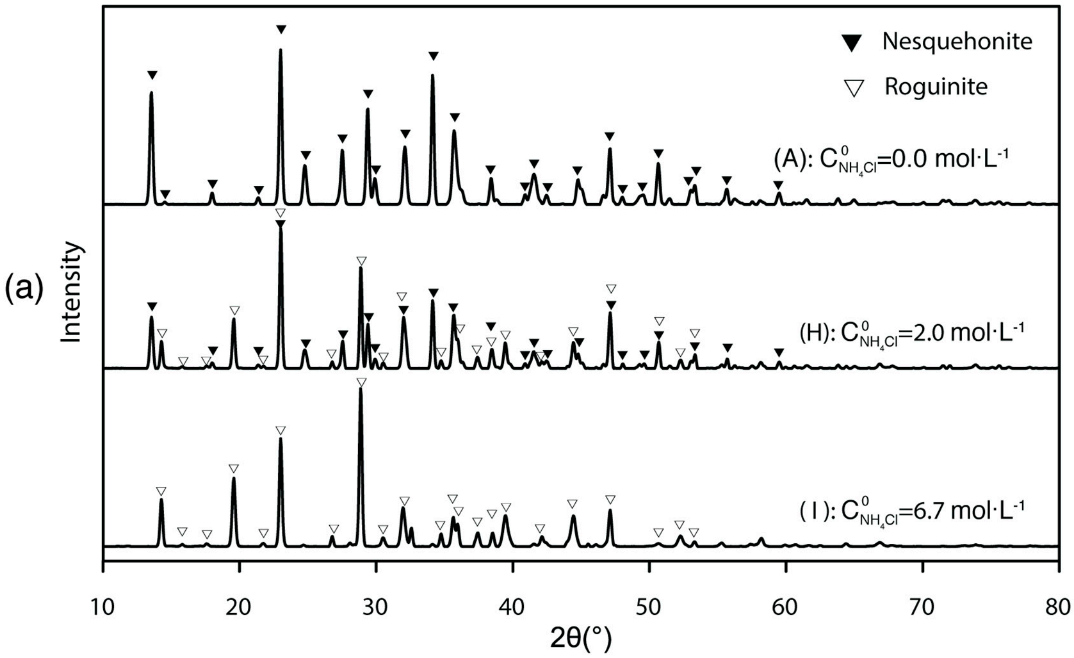

Figure 5. *Cont.*

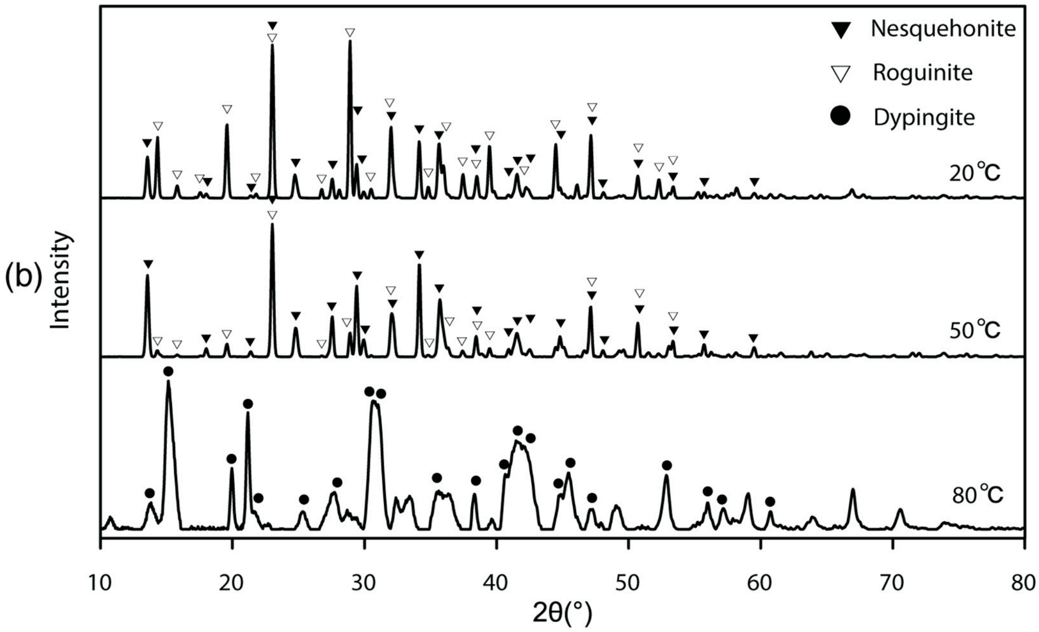

Figure 5. X-ray diffraction patterns of solid samples: (**a**) Mg-carbonate precipitated under various initial NH_4Cl concentrations; (**b**) Mg-carbonate separated after washing in water for 1 h at different temperatures.

4. Discussion

In this section, we first simulate the temporal evolution of solution components under constant pH conditions to detail solution chemistry. We next build a model to link solution chemistry to CO_2 absorption rate, and use the model to discuss the CO_2 absorption kinetics quantitatively. Finally, we discuss Mg-carbonate precipitation kinetics and the mineral forms of the products.

4.1. Modeling of Solution Chemistry and Temporal Evolution

To characterize the dynamic nature of the reaction, the temporal evolution of primary and secondary species during experiments is simulated using the PHREEQC program. Several parameters are imported: (1) DIC concentration values, which are calculated by subtracting precipitated carbon from TC before passed to PHREEQC program. Since Mg/C ratio in nesquehonite structure is 1:1, precipitated carbon can be calculated through subtracting measured Mg concentrations from initio Mg concentration; (2) Concentrations of Cl, which are set to double the initial Mg concentration; (3) Measured Mg concentrations in solution; (4) Measured pH values; (5) With the knowledge of DIC, Mg, and Cl concentrations and pH, the concentration of total ammonium nitrogen (TN) can be calculated through charge balance. Finally, solution speciation equations are solved automatically by PHREEQC.

Figure 6 shows the modeled temporal evolution curves of the solution species, with pH maintained at 9.00 and the initial Mg concentration set as 0.10 $mol \cdot L^{-1}$, a scenario where nesquehonite appears (experiment C). Before precipitation, the major cation in the solution is Mg^{2+}, followed by NH_4^+ (the dominant contributor to the total ammonium nitrogen) (Figure 6b,c). The main carbon species is HCO_3^- followed by $MgCO_3^0$, $MgHCO_3^+$, and CO_3^{2-}. The main anion is Cl^-. Nesquehonite reaches saturation rapidly, but its precipitation does not occur until ~2.5 h after the beginning of the reaction (Figure 6d). Although the modeled results also suggest that the solution became oversaturated rapidly after absorption, such a long time for the appearance of crystal indicates slow nucleation. Upon precipitation, the Mg^{2+} concentration in the solution decreases rapidly, together with HCO_3^-, $MgCO_3^0$ and CO_3^{2-}, and NH_4^+ becomes the dominant cation. At this stage, addition of ammonia is required to neutralize the H^+ produced by the removal of CO_3^{2-} (Equation (13)), to maintain the pH. As the precipitation continues, the concentrations of HCO_3^- and CO_3^{2-} gradually recover but not the

Mg-related species (Figure 6a,b). Throughout the whole course of the experiments, brucite remains undersaturated (Figure 6d), indicating a successful control of the solution composition. Based on the discussion above, the overall reaction in solution for experiments A–G appears to be:

$$NH_3 + Mg^{2+} + HCO_3^- + 3H_2O \leftrightarrow NH_4^+ + MgCO_3{\cdot}3H_2O\downarrow \quad (18)$$

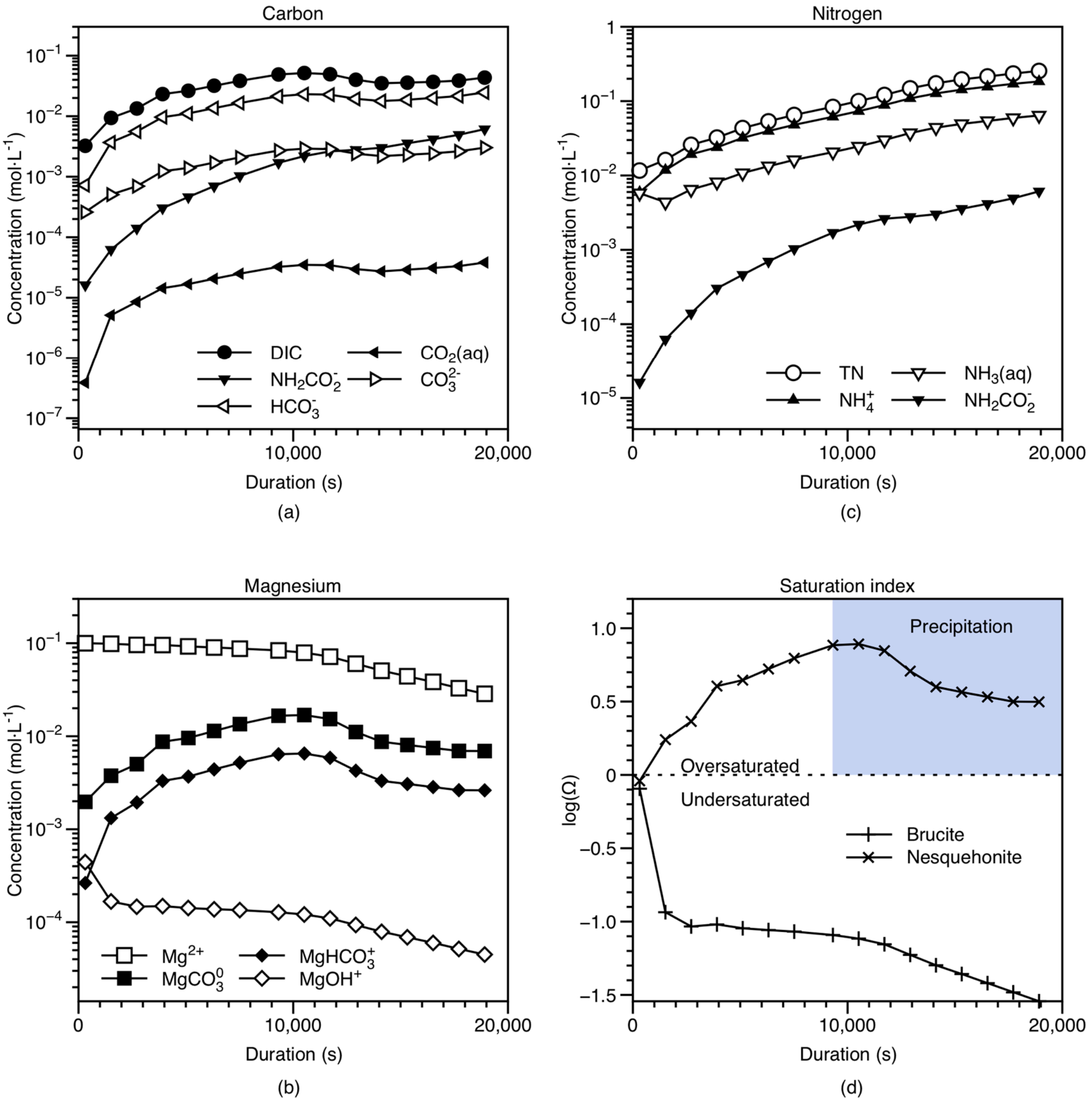

Figure 6. Temporal evolution of solution chemistry from experiment C: (**a**) Concentration of carbonic species; (**b**) concentration of magnesium species; (**c**) concentration of ammonium species; (**d**) SI of nesquehonite and brucite.

4.2. Gas-Solution Interface Kinetics

4.2.1. Reaction Kinetics between CO_2 and NH_3

To characterize the reaction kinetics at the gas-solution interface, here we consider the physical and chemical processes of CO_2 mass transfer from gas phase to solution. After transporting CO_2 into solution, three reactions can promote the transformation of molecular CO_2(aq) to HCO_3^- (Equations (1)–(3)). Since the concentration of water is a constant, and the solution pH is fixed, the reaction rates of Equations (1) and (2) should be constant, i.e., CO_2 absorption rate should be stable in a pH-controlled NaOH solution (experiment X, Figures 3a and 4a). In contrast, CO_2 absorption rates in NH_3 solutions exhibit an increasing trend even with a fixed solution pH. The enhanced CO_2 absorption rates in NaOH versus NH_3 solutions can be explained by the promotion of reaction kinetics, as shown by Equation (3), likely as the result of an increasing concentration of NH_3(aq) (Figure 6c).

The reaction mechanism of Equation (3) discussed in Section 1.2 yielded a complex kinetic expression (Equation (11)), with up to five rate constants. To reduce the computational complexity, the reaction is simplified to a second-order reaction. Consequently, Equation (11) is simplified to:

$$r_{\mathrm{CO_2-NH_3}} = k_{\mathrm{app}} C_{\mathrm{CO_2}} C_{\mathrm{NH_3}}, \tag{19}$$

where k_{app} is the apparent kinetic constant of Equation (3).

To link the CO_2 absorption rate to reaction kinetics, a "two-film" model is adopted to describe the mass transfer process. Figure 7 illustrates the concept of this model. In essence, the diffusion film on the gas side and the solution side determine the efficiency of mass transfer. In this framework, the rate of CO_2 absorption ($\varphi_{\mathrm{CO_2}}$) can be written as:

$$\varphi_{\mathrm{CO_2}} = k_{\mathrm{ov}} \Delta P_{\mathrm{CO_2}} \approx k_{\mathrm{ov}} P_{\mathrm{CO_2}}^{\mathrm{bulk}} \tag{20}$$

and

$$\frac{1}{k_{ov}} = \frac{1}{k_g} + \frac{1}{k_l}, \tag{21}$$

where $\Delta P_{\mathrm{CO_2}}$ is the pressure gradient of CO_2 from bulk gas phase to bulk solution, and k_{ov} is the overall mass transfer coefficient. k_{ov} consisted of a gas-side (k_g) and solution-side (k_l) mass transfer coefficient, and their reciprocal forms represent mass transfer resistance at the gas side and solution side, respectively (Equation (21)). The magnitude of k_g is determined by fluid properties of the gas phase, which has been calibrated by previous studies [57]. In the two-film model, an enhancement factor (E) is used to describe the mass transfer accelerated by a chemical reaction on the solution side (i.e., the solution-side mass transfer coefficient with reactions (k_l) versus physical mass transfer coefficient with no chemical reaction (k_l^0)). Methods to calculate k_l^0 can be found elsewhere [40]. Table 3 lists the experimental results of the enhancement factor (E_{exp}) at different sampling times. To link reaction kinetics to E, two additional parameters, the Hatta modulus (M_H^2) and an enhancement factor for an infinitely fast reaction (E_i), are introduced below:

$$M_H^2 = \frac{k_{total} D_{\mathrm{CO_2,L}}}{(k_l^0)^2} \tag{22}$$

$$k_{total} = k_{\mathrm{H_2O}} C_{\mathrm{H_2O}} + k_{\mathrm{OH^-}} C_{\mathrm{OH^-}} + k_{app} C_{\mathrm{NH_3}} \tag{23}$$

$$E_i = 1 + \frac{D_{\mathrm{NH_3,L}} C_{\mathrm{NH_3}} H_{\mathrm{CO_2}}}{D_{\mathrm{CO_2,L}} P_{\mathrm{CO_2}}^{int}}, \tag{24}$$

where $D_{\mathrm{CO_2,L}}$ is the diffusion coefficient of CO_2 in the liquid phase, $D_{\mathrm{NH_3,L}}$ and $C_{\mathrm{NH_3}}$ are the diffusion coefficient and the bulk concentration of ammonia in the liquid phase, respectively, and $P_{\mathrm{CO_2}}^{int}$ is the partial pressure of CO_2 in the liquid phase at the gas-liquid interface. Although, $D_{\mathrm{CO_2,L}}$ and $D_{\mathrm{NH_3,L}}$ are inversely proportional to solution viscosity (i.e., the Stokes–Einstein equation), which is a function of solution composition and temperature. The diffusion coefficient of CO_2 and NH_3 in water at 25 °C is used as approximation of diffusion in NH_3–$MgCl_2$ solutions due to the limited concentration effect on viscosity [70]. To calculate the theoretical enhancement factor (E_{cal}), we refer to an explicit approximate expression [71]:

$$E_{cal} = -\frac{M_H^2}{2(E_i - 1)} + \sqrt{\frac{M_H^4}{4(E_i - 1)^2} + \frac{E_i M_H^2}{E_i - 1} + 1}. \tag{25}$$

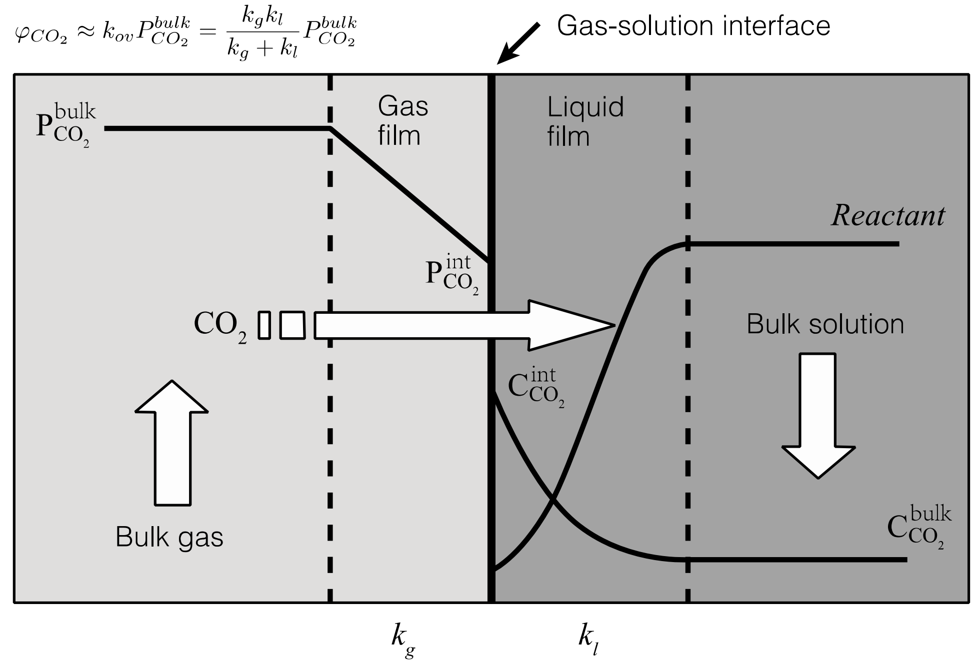

Figure 7. A schematic diagram of CO_2 mass transfer process from gas phase to solution. Gas and solution diffusion film are on both sides of the interface, respectively, limiting the CO_2 absorption rate (φ_{CO_2}). In this work, the pressure gradient (ΔP_{CO_2}) is approximated to the bulk pressure ($P_{CO_2}^{bulk}$) due to neglectable CO_2(aq) concentration ($C_{CO_2}^{bulk}$, ~10^{-5} mol·L^{-1}) in solution under experimental pH ranges.

Table 3. Solution chemistry and CO_2 absorption kinetics data for experiments C and E–G.

ID	Time	pH	TN	$C_{NH_3(aq)}$	DIC	C_{Mg}	k_{ov}	k_l	E_{exp}	E_{cal}
	s		mol·L^{-1}				$\times 10^{-7}$mol·m^{-2}·Pa^{-1}·s^{-1}			
E	406	9.146	0.007	0.002	0.003	0.103	0.51	0.52	1.38	1.50
	2206	8.771	0.017	0.003	0.008	0.102	0.44	0.45	1.19	1.50
	4006	8.761	0.027	0.004	0.015	0.102	0.44	0.45	1.19	1.53
	5806	8.786	0.041	0.007	0.022	0.101	0.58	0.60	1.57	1.60
	7606	8.755	0.058	0.009	0.030	0.101	0.58	0.60	1.57	1.68
	9406	8.715	0.059	0.009	0.041	0.105	0.58	0.60	1.57	1.64
	11,206	8.763	0.075	0.012	0.046	0.102	0.58	0.60	1.57	1.72
	12,406	8.760	0.092	0.015	0.051	0.102	0.58	0.60	1.57	1.81
	13,606	8.776	0.110	0.018	0.055	0.099	0.65	0.67	1.77	1.90
	14,806	8.784	0.109	0.018	0.060	0.099	0.65	0.67	1.77	1.87
	16,006	8.753	0.130	0.020	0.065	0.098	0.65	0.67	1.77	1.95
	17,206	8.731	0.151	0.023	0.062	0.089	0.65	0.67	1.77	2.01
	18,406	8.747	0.149	0.023	0.057	0.078	0.65	0.67	1.77	1.98
	19,606	8.746	0.212	0.033	0.054	0.068	0.65	0.67	1.77	2.25
	20,806	8.766	0.184	0.030	0.053	0.062	0.65	0.67	1.77	2.13
	22,006	8.765	0.217	0.035	0.051	0.056	0.65	0.67	1.77	2.25
C	316	9.456	0.015	0.007	0.003	0.102	0.54	0.56	1.47	1.71
	1516	9.038	0.020	0.005	0.009	0.103	0.54	0.56	1.47	1.62
	2716	8.996	0.033	0.008	0.013	0.102	0.54	0.56	1.47	1.70
	3916	9.004	0.039	0.010	0.023	0.107	0.54	0.56	1.47	1.72
	5116	8.999	0.059	0.015	0.026	0.105	0.54	0.56	1.47	1.89
	6316	8.999	0.068	0.017	0.032	0.105	0.61	0.63	1.66	1.91
	7516	9.000	0.098	0.024	0.038	0.105	0.68	0.71	1.86	2.14

Table 3. *Cont.*

ID	Time	pH	TN	$C_{NH_3(aq)}$	DIC	C_{Mg}	k_{ov}	k_l	E_{exp}	E_{cal}
	s		mol·L^{-1}				×10^{-7}mol·m^{-2}·Pa^{-1}·s^{-1}			
C	9316	8.999	0.107	0.026	0.049	0.105	0.75	0.78	2.05	2.12
	10,516	8.999	0.149	0.036	0.052	0.101	0.75	0.78	2.05	2.38
	11,716	9.000	0.156	0.038	0.049	0.092	0.82	0.86	2.25	2.36
	12,916	8.999	0.169	0.042	0.040	0.075	0.90	0.93	2.46	2.39
	14,116	9.000	0.186	0.047	0.035	0.062	0.90	0.93	2.46	2.46
	15,316	9.000	0.254	0.063	0.036	0.054	0.90	0.93	2.46	2.79
	16,516	8.998	0.255	0.064	0.037	0.048	0.82	0.86	2.25	2.77
	17,716	9.000	0.273	0.069	0.039	0.042	0.90	0.93	2.46	2.84
	18,916	9.000	0.297	0.074	0.043	0.038	0.90	0.93	2.46	2.92
F	263	9.485	0.012	0.006	0.003	0.102	0.58	0.60	1.58	1.60
	1463	9.172	0.024	0.008	0.008	0.102	0.51	0.53	1.39	1.70
	2663	9.161	0.034	0.011	0.014	0.102	0.58	0.60	1.58	1.72
	3863	9.161	0.048	0.016	0.019	0.102	0.65	0.67	1.77	1.84
	5063	9.155	0.069	0.022	0.025	0.102	0.65	0.67	1.77	2.02
	6263	9.164	0.096	0.031	0.031	0.101	0.72	0.75	1.97	2.23
	7463	9.155	0.090	0.029	0.041	0.104	0.87	0.90	2.37	2.11
	8663	9.164	0.130	0.042	0.047	0.102	0.87	0.90	2.37	2.41
	9863	9.157	0.110	0.035	0.056	0.102	0.94	0.98	2.58	2.19
	11,063	9.162	0.151	0.048	0.058	0.096	1.01	1.06	2.78	2.47
	12,263	9.154	0.145	0.046	0.056	0.084	1.08	1.14	3.00	2.38
	13,463	9.155	0.183	0.059	0.052	0.069	1.16	1.22	3.21	2.61
	14,663	9.160	0.250	0.080	0.052	0.060	1.23	1.30	3.43	2.98
	15,863	9.165	0.347	0.111	0.054	0.050	1.30	1.39	3.65	3.43
	17,063	9.158	0.341	0.108	0.059	0.044	1.38	1.47	3.87	3.37
	18,263	9.158	0.356	0.112	0.067	0.039	1.38	1.47	3.87	3.41
G	179	9.460	0.009	0.005	0.002	0.091	0.52	0.53	1.40	1.57
	1979	9.703	0.052	0.033	0.010	0.089	0.88	0.91	2.40	2.16
	3779	9.690	0.130	0.081	0.026	0.091	1.17	1.24	3.26	3.01
	4979	9.696	0.152	0.095	0.035	0.089	1.40	1.49	3.93	3.15
	6179	9.690	0.260	0.161	0.043	0.084	1.63	1.76	4.63	3.97
	7379	9.700	0.315	0.197	0.042	0.068	1.87	2.04	5.37	4.31
	8579	9.689	0.370	0.229	0.045	0.054	2.11	2.34	6.14	4.60
	9779	9.693	0.417	0.257	0.055	0.045	2.28	2.54	6.68	4.83
	10,979	9.693	0.557	0.338	0.067	0.037	2.45	2.75	7.24	5.50
	13,979	9.699	0.815	0.477	0.110	0.024	2.79	3.19	8.41	6.47

Since Equations (22)–(25) only contain one variable k_{app}, one can fit E_{cal} to E_{exp} by tuning this parameter. Fitting results show that E_{exp} can be reproduced satisfactorily using the models built above (Figure 8), but notable deviations exist when E_{exp} is larger than 4. Table 4 shows the fitted k_{app} value together with the values compiled from other studies. The k_{app} value obtained in this work is similar to but slightly higher than in earlier studies conducted at relatively low NH_3 concentrations [62,72]. Concerning the deviations in Figure 8a, it should be noted that we assume a constant k_{app} in the fitting; in reality, however, k_{app} may vary when conditions change. Specifically, due to accelerated deprotonating (Equation (8)), the overall rate constant between CO_2 and NH_3 (Equation (11)) is expected to correlate positively with the NH_3 concentration. Thus, k_{app} should increase with NH_3 concentration. Such dependency is also shown by the observation of greater k_{app} under higher NH_3 concentrations in previous work [40,73] (Table 4).

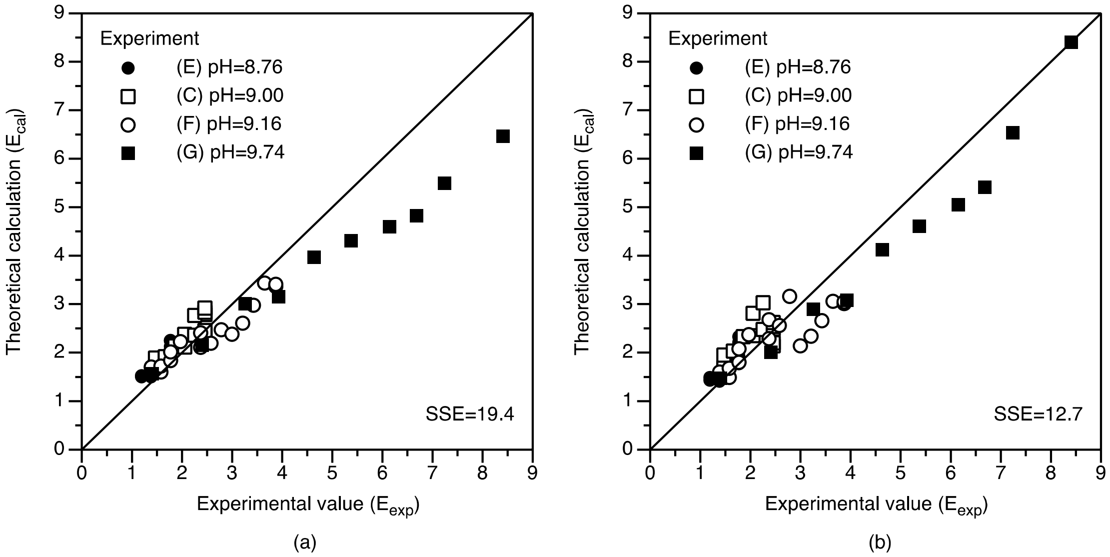

Figure 8. Experimental enhancement factor (E_{exp}) vs theoretical calculation (E_{cal}): (**a**) fixed k_{app}; (**b**) linear relationship with $C_{NH_3(aq)}$.

Table 4. Comparison of kinetic constants in the literature at 25 °C.

$C_{NH_3(aq)}$	T	k_{app}[1]	k_2[2]	Sources
mol·L^{-1}	°C	m^3·mol^{-1}·s^{-1}		
0.027–0.19	0–40	0.44	-	[72]
0.002–0.016	15–45	0.45	-	[62]
0.1–7	5–25	0.37–1.30	12.8	[39]
0.9–5.4	25–49	0.94–0.95	1.23×10^7	[73]
0.6–5.6	6–31	0.95–1.14	59.0	[40]
0.002–0.62	25	0.32–0.95	-	This work

[1] Apparent kinetic rate constant between CO_2 and $NH_3(aq)$ within concentration range in this work ($C_{NH_3(aq)} = 0.002–0.62$ mol·L^{-1}); [2] Rate constant of zwitterion formation reaction (Equation (7)).

Knowing k_{app}'s dependence on NH_3 concentration, we now refine the calculation of the theoretical enhancement factor (E_{cal}) by assuming a linear relationship between C_{NH_3} and k_{app} $\left(m^3 \cdot mol^{-1} \cdot s^{-1}\right)$:

$$k_{app} = 1.022\, C_{NH_3} + 0.414. \tag{26}$$

The intercept and slope of Equation (26) are obtained through fitting E_{cal} to E_{exp} With this correction, the fit between E_{exp} and E_{cal} is significantly improved (with a smaller sum of squared errors, or SSE), especially when $E_{exp} > 4$ (Figure 8). Notably, the linear form of Equation (26) is similar to the rate constant expression of Equation (3) developed within a "termolecular mechanism" frame, where the initial product is not zwitterions but a loosely bounded termolecular complex involving CO_2, ammonia, and base molecules [73–75].

4.2.2. Factors Controlling CO_2 Absorption

In the two-film model, the mass transfer coefficients on the gas side (k_g) and the solution side (k_l) are important factors controlling the CO_2 absorption rate under a fixed pressure gradient. Since the gas phase fluid dynamic parameters directly determine k_g, the gas phase fluid conditions are kept the same ($k_g = 2.23 \times 10^{-6}$ mol·m^{-2}·Pa^{-1}·s^{-1}) between all absorption experiments. The much higher k_g values, as compared to experimental k_l values ($0.45 - 3.19 \times 10^{-7}$ mol·m^{-2}·Pa^{-1}·s^{-1}, Table 3), indicate that the mass transfer in solution side is the slow step for CO_2 absorption in the wetted-column device.

Thus, an absorption device designed with high k_l values (e.g., bubble tank) should be able to promote CO_2 mass transfer through $MgCl_2$–NH_3–NH_4Cl solutions.

As discussed in Section 4.2.1, three reactions (Equations (1)–(3)) are contributing to CO_2 mass transfer on the solution side. Figure 9a shows the individual rate constant of these reactions in a pseudo first-order form (i.e., $k_xC_x = k_{H_2O}C_{H_2O} = k'_{H_2O}$ for H_2O; $k_xC_x = k_{OH^-}C_{OH^-}$ for OH^-; $k_xC_x = k_{app}C_{NH_3}$ for NH_3). The rate constant of Equation (1) is fixed at 0.026 s^{-1} for experiments C, E, F, and G as we set the temperature and water concentration to be constant. Similarly, the rate constant of Equation (2) for any specific experiment is constant, but shows a positive correlation with solution pH among the different experiments (from 0.064 s^{-1} of experiment E, to 0.615 s^{-1} of G). The rate constant of OH^- is ~3–30 times larger than H_2O. The rate constant of NH_3(aq) is highest, up to 431 s^{-1}(Figure 9a), thus the CO_2–NH_3 reaction should be the dominant reaction among reactions (1)–(3). As discussed in Section 4.2.1, the reaction rate between CO_2(aq) and NH_3(aq) increases with NH_3(aq) concentration through enhanced reaction rate and greater apparent rate constant k_{app} (Equations (19) and (26), Figure 9b). Thus, higher NH_3(aq) concentration would facilitate CO_2 mass transfer on the solution side, either through increasing the total ammonium nitrogen concentration (e.g., adding ammonium salts) or raising the pH.

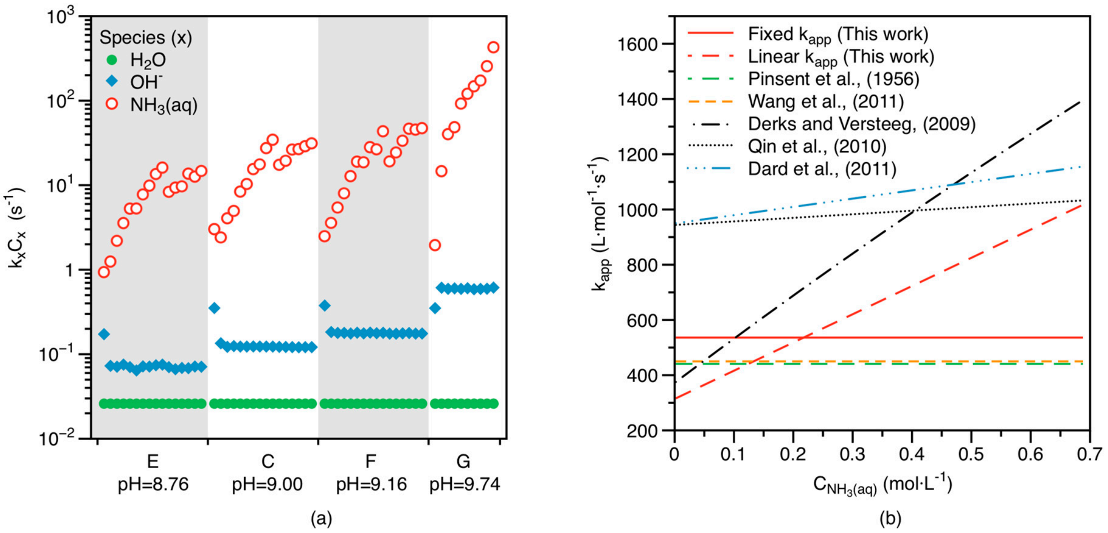

Figure 9. Factors that affect CO_2 reaction kinetics in the liquid side: (**a**) Rate contribution of H_2O, OH^- and NH_3(aq) to CO_2 consumption in solution-side diffusive film. k_xC_x represents the pseudo first-order rate constant of species x to react with CO2. (**b**) Various dependency of k_{app} on NH_3(aq) concentration.

Although the effect of temperature is not investigated in this work, its effect on CO_2 absorption is expected to be positive (i.e., higher temperature, faster CO_2 absorption), as shown by previous studies (e.g., [40,73]).

4.3. Mg-carbonate Precipitation and Phase Transformation

4.3.1. Nesquehonite Precipitation Kinetics

Our results show that Mg-carbonate only precipitates as nesquehonite (Table 1) in the absence of NH_4Cl. We further discuss the effect of nesquehonite precipitation on CO_2 absorption.

The initial Mg concentration does not affect the CO_2 absorption process (Figure 3) but impacts on carbonate precipitation (e.g., timing of nesquehonite's first appearance). Figure 10 shows the amount of total absorbed carbon (as CO_2) and precipitated carbon (as nesquehonite). Although CO_2 transfers from gas phase to solution continuously, precipitation does not start until a certain time point (Figure 6d). At this stage, the solution quickly becomes supersaturated (relative to nesquehonite), overcomes the nucleation energy barrier, and starts precipitating carbonate. The initial precipitation rate of nesquehonite (φ_p) is smaller compared to the CO_2 absorption rate (φ_{CO_2}), making the absorbed CO_2 accumulate in the solution as dissolved inorganic carbon (DIC) (Figure 10a,b). After initial precipitation, φ_p increases rapidly and overwhelms φ_{CO_2}, efficiently converting DIC to nesquehonite. By default, no further Mg is added into the reactor. As a result, the solution gradually gets less saturated, and φ_p becomes smaller than φ_{CO_2} again, leading to increasing DIC. The accumulation of DIC in the solution also reduces the CO_2-carbonate conversion efficiency.

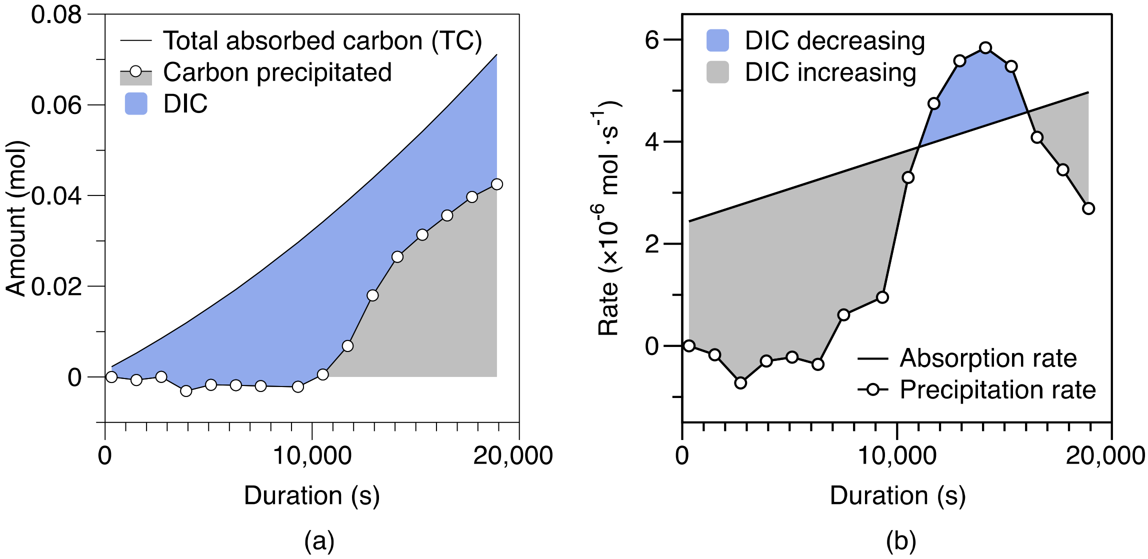

Figure 10. Rate of CO_2 absorption (φ_{CO_2}) and nesquehonite precipitation (φ_p) in experiment C: (**a**) Temporal evolution of amount of CO_2 absorbed and nesquehonite precipitated. The space between two lines is the amount of CO_2 preserved in the solution as DIC. (**b**) Rate of absorption vs precipitation. CO_2 is efficiently converted to nesquehonite when $\varphi_p > \varphi_{CO_2}$.

Based on the above highlighted observations, we suggest that the concentration of Mg in solution needs to be controlled for enhanced CO_2-carbonate transformation efficiency. In industrial practices, timely input of concentrated-Mg solutions should be exercised to guarantee the condition of $\varphi_p > \varphi_{CO_2}$. Nucleation barrier is another concern during industrialization, as the relatively long induction time of nesquehonite (1.2–3.6 h, Sections 3.1 and 3.2) indicates quite a high nucleation energy barrier. The addition of crystal seeds might help to overcome such an energy threshold.

Besides nucleation, nesquehonite precipitation experiments conducted in the literature under similar CO_2 partial pressure by spraying gas into brucite slurry [34] exhibited a smaller precipitation rate (~0.01 mol·L^{-1}·h^{-1}, P_{CO_2} = 0.1 atm) compared to this work (~0.04 mol·L^{-1}·h^{-1}, P_{CO_2} = 0.15 atm), indicating the kinetic advancement of our process. On the other hand, brucite carbonation under elevated pressure (15 atm) resulted in a much higher precipitation rate (~0.66 mol·L^{-1}·h^{-1}) [76]. Overall, due to quite different technical settings, we could only do a first-order comparison, but further studies are needed to normalize the effects of scales and other factors (e.g., CO_2 pressure and gas-solution contact area) for a more meaningful comparison.

4.3.2. Phase Transformation of Less Stable to More Stable Carbonation Products

The chief Mg-carbonate precipitated under high TN conditions (>2 mol·L^{-1}) is roguinite, which was formed by milling epsomite ($MgSO_4{\cdot}7H_2O$) with NH_4HCO_3 [77]. Roguinite is very unstable under ambient conditions and can lose all of the ammonium carbonate and most of the water, forming amorphous magnesium carbonate with a very high surface area (~500 m^2·g^{-1}) via thermal decomposition [78]. Our results show that roguinite can be transformed into nesquehonite at 50 °C and further converted to dypingite at 80 °C by washing with water. During phase transformation, the ammonium component is also removed from the solid, allowing for recycling for CO_2 absorption.

Under low TN conditions (<2 mol·L^{-1}), nesquehonite is the dominant Mg-carbonate precipitated besides roguinite. Nesquehonite is also unstable at ambient conditions and can gradually lose CO_2, transforming to its basic form (e.g., dypingite and hydromagnesite) at temperatures above 50 °C [36,55] or even at room temperature [34,79]. Thus, once washed in hot water (>50 °C), both nesquehonite and roguinite can be transformed into basic magnesium carbonates.

4.4. Implications for Industrial Applications

Experimental data show that liquid-side mass transfer process is the rate-limiting step of CO_2 absorption. Thus, to achieve more efficient CO_2 scrubbing, reactors with a higher liquid-side mass transfer coefficient, k_l^0, are needed. Various kinds of reactors are available for the CO_2 absorption depending on how the gas is in contact with the solution/slurry [80]. For aqueous droplets falling in the gas phase, i.e., spray tower, the gas phase side has a lower mass transfer barrier due to stronger gas phase convection. Thus, a spray tower is suitable for fast reaction systems, e.g., SO_2 absorption. On the other hand, for the liquid-side mass transfer limited CO_2–$MgCl_2$–NH_3–NH_4Cl system, letting the gas phase rise within the solution (i.e., bubbling) would guarantee a more effective liquid-side mass transfer process. Thus, a bubble tank is an ideal reactor and works better with agitation. Besides the economic advantages, a bubbled tank with agitation can handle solid precipitation without being clogged up, compared with staged tower reactors. In addition, similar to this study, parameters including NH_3 concentration, Mg concentration, and pH can also be tuned to fulfill a CO_2 emissions reduction target.

Phase transformation experiments show that an unstable form of nesquehonite or roguinite can be readily converted to stable basic-form Mg-carbonates (dypingite in this study), which are important industrial raw materials with diverse applications. Dypingite-like Mg-carbonates can serve as a flame-retardant or fire-retardant additive for polymers [81–83] or simply as backfill [84]. Hydromagnesite is also a promising material to replace CaO in calcium-based cement, which usually has a net release of CO_2, as opposed to Mg-based cement, which could potentially absorb nearly as much CO_2 during its service life as was emitted during its manufacture (carbon-neutral) [85].

Since the working medium used for CO_2 absorption is Mg solution in this study, a broad range of Mg-rich minerals could act as a raw material. Thus, the theoretical sequestration ability is almost unlimited. However, considering the tremendous energy that goes into harvesting Mg from silicates [11], Mg-containing brines resulting from silicate weathering might be more promising. For example, the Qinghai Lake (water capacity 119.6 km^3) in western China has an extremely high Mg concentration of 16 g·L^{-1} [86], which could sequestrate 3.5 Gt CO_2 in total while producing 9.3 Gt hydromagnesite. In addition, a solid byproduct of potassium salt production named bischofite ($MgCl_2 \cdot 6H_2O$) is readily available for use. Notably, 320–480 Mt of bischofite are produced each year around Chaidam basin in China [87], equivalent to a CO_2 sequestration potential of 70–104 Mt producing 186–276 Mt hydromagnesite.

5. Conclusions

This study systematically investigated the reaction kinetics of CO_2 absorption and Mg-carbonate precipitation in $MgCl_2$–NH_3–NH_4Cl solutions using a novel pH-controlled wetted-wall column device. The obtained results from and conclusions about the studied system are summarized as follows:

(1) Careful design and theoretical modeling of solution chemistry led to the precipitation of high-purity nesquehonite in NH_4Cl-free experiments.

(2) The gas-side and liquid-side mass transfer coefficients were estimated through combining experimental data and a two-film mass transfer model. Notably, the CO_2 mass transfer resistance on the liquid side was found to be greater than the gas side, suggesting that the liquid-side

reaction is the major limiting step in the overall reaction and that a higher liquid-side mass transfer coefficient should promote CO_2 absorption.

(3) Interaction of CO_2(aq) with NH_3(aq) is a critical process controlling CO_2 mass transfer from the gas to the solid phase. Based on the zwitterion mechanism, NH_3(aq) concentration correlates closely with the apparent rate constant of the CO_2–NH_3(aq) reaction (k_{app}), pointing to the importance of NH_3 in the overall reaction. Together with the literature data, our results suggest that increasing temperature, pH, and NH_3(aq) concentration would facilitate CO_2 absorption.

(4) The solid products are sensitive to ambient conditions and treatments. If the initial ammonium nitrogen concentration is low ($C^0_{NH_4Cl} < 2\ mol \cdot L^{-1}$), only nesquehonite would precipitate; if $C^0_{NH_4Cl} > 2\ mol \cdot L^{-1}$, roguinite would appear. High pH value and high Mg concentration could help nesquehonite overcome the nucleation energy barrier and facilitate carbonation. Thus, besides adjusting pH, adding dissolved Mg is likely an effective way to enhance the precipitation rate of Mg-carbonate.

(5) Industrially useful and more stable materials could be obtained with designed treatments of the solid products. Specifically, washing nesquehonite and roguinite in hot water (>50 °C) could convert those minerals to more basic forms of Mg-carbonate (e.g., dypingite).

Overall, our work provides a more comprehensive understanding of the kinetics of a carbonation reaction in the $MgCl_2$–NH_3–NH_4Cl system, which would allow for the development of an applicable CO_2-minimization routine. The studied factors and their associated behavior can directly guide the design and optimization of reaction systems aiming at more efficient CO_2–Mg-carbonate conversion, and help with building facilities for capturing and sequestering atmospheric CO_2 at the industrial scale.

Acknowledgments: The authors wish to thank the three anonymous reviewers for their constructive suggestions. This work was funded by the National Natural Science Foundation of China (Grant Nos. 41002014 and 41273075) to L.Z. and the Office of Basic Energy Science, U.S. DOE, through Grant No. DE-FG02-02ER15366 to H.T.

Author Contributions: C.Z. conceived and designed the experiments; C.Z., H.W., X.D., and S.A. performed the experiments; C.Z., H.W., X.D., and S.A. analyzed the data; L.Z. contributed reagents/materials/analysis tools; C.Z. wrote the paper; G.L., L.Z., and H.H.T. revised the paper.

Conflicts of Interest: The authors declare no conflict of interest. The founding sponsors had no role in the design of the study; in the collection, analyses, or interpretation of data; in the writing of the manuscript; or in the decision to publish the results.

References

1. Seifritz, W. CO_2 disposal by means of silicates. *Nature* **1990**, *345*, 486. [CrossRef]
2. Park, A.-H.A.; Fan, L.-S. Mineral sequestration: Physically activated dissolution of serpentine and pH swing process. *Chem. Eng. Sci.* **2004**, *59*, 5241–5247. [CrossRef]
3. Béarat, H.; McKelvy, M.J.; Chizmeshya, A.V.G.; Gormley, D.; Nunez, R.; Carpenter, R.W.; Squires, K.; Wolf, G.H. Carbon Sequestration via Aqueous Olivine Mineral Carbonation: Role of Passivating Layer Formation. *Environ. Sci. Technol.* **2006**, *40*, 4802–4808. [CrossRef] [PubMed]
4. Intergovernmental Panel on Climate Change (IPCC). *IPCC Special Report on Carbon Dioxide Capture and Storage*; Cambridge University Press: Cambridge, UK, 2006; ISBN 978-0-521-68551-1.
5. White, A.F.; Brantley, S.L. The effect of time on the weathering of silicate minerals: Why do weathering rates differ in the laboratory and field? *Chem. Geol.* **2003**, *202*, 479–506. [CrossRef]
6. O'Connor, W.K.; Dahlin, D.C.; Nilsen, D.N.; Gerdemann, S.J.; Rush, G.E.; Penner, L.R.; Walters, R.P.; Turner, P.C. *Continuing Studies on Direct Aqueous Mineral Carbonation of CO_2 Sequestration*; Albany Research Center: Albany, OR, USA, 2002.
7. O'Connor, W.K.; Dahlin, D.C.; Rush, G.E.; Gedermann, S.J.; Penner, L.R.; Nilsen, D.N. *Aqueous Mineral Carbonation*; Albany Research Center: Albany, OR, USA, 2005.
8. Rigopoulos, I.; Vasiliades, M.A.; Ioannou, I.; Efstathiou, A.M.; Godelitsas, A.; Kyratsi, T. Enhancing the rate of ex situ mineral carbonation in dunites via ball milling. *Adv. Powder Technol.* **2016**, *27*, 360–371. [CrossRef]

9. Park, A.-H.A.; Jadhav, R.; Fan, L.-S. CO_2 Mineral Sequestration: Chemically Enhanced Aqueous Carbonation of Serpentine. *Can. J. Chem. Eng.* **2003**, *81*, 885–890. [CrossRef]
10. Andreani, M.; Luquot, L.; Gouze, P.; Godard, M.; Hoisé, E.; Gibert, B. Experimental Study of Carbon Sequestration Reactions Controlled by the Percolation of CO_2-Rich Brine through Peridotites. *Environ. Sci. Technol.* **2009**, *43*, 1226–1231. [CrossRef] [PubMed]
11. Huijgen, W.J.J.; Comans, R.N.J. *Carbon Dioxide Sequestration by Mineral Carbonation: Literature Review*; Energy Research Centre of the Netherlands ECN: Petten, The Netherlands, 2003.
12. Azdarpour, A.; Asadullah, M.; Junin, R.; Manan, M.; Hamidi, H.; Daud, A.R.M. Carbon Dioxide Mineral Carbonation Through pH-swing Process: A Review. *Energy Procedia* **2014**, *61*, 2783–2786. [CrossRef]
13. Azdarpour, A.; Asadullah, M.; Mohammadian, E.; Hamidi, H.; Junin, R.; Karaei, M.A. A review on carbon dioxide mineral carbonation through pH-swing process. *Chem. Eng. J.* **2015**, *279*, 615–630. [CrossRef]
14. Rudnick, R.L.; Gao, S. Composition of the Continental Crust. *Treatise Geochem.* **2003**, *3*, 659. [CrossRef]
15. Van Essendelft, D.T.; Schobert, H.H. Kinetics of the Acid Digestion of Serpentine with Concurrent Grinding. 1. Initial Investigations. *Ind. Eng. Chem. Res.* **2009**, *48*, 2556–2565. [CrossRef]
16. Van Essendelft, D.T.; Schobert, H.H. Kinetics of the Acid Digestion of Serpentine with Concurrent Grinding. 2. Detailed Investigation and Model Development. *Ind. Eng. Chem. Res.* **2009**, *48*, 9892–9901. [CrossRef]
17. Van Essendelft, D.T.; Schobert, H.H. Kinetics of the Acid Digestion of Serpentine with Concurrent Grinding. 3. Model Validation and Prediction. *Ind. Eng. Chem. Res.* **2010**, *49*, 1588–1590. [CrossRef]
18. Hariharan, S.B.; Werner, M.; Zingaretti, D.; Baciocchi, R.; Mazzotti, M. Dissolution of Activated Serpentine for Direct Flue-Gas Mineralization. *Energy Procedia* **2013**, *37*, 5938–5944. [CrossRef]
19. Farhang, F.; Rayson, M.; Brent, G.; Hodgins, T.; Stockenhuber, M.; Kennedy, E. Insights into the dissolution kinetics of thermally activated serpentine for CO_2 sequestration. *Chem. Eng. J.* **2017**, *330*, 1174–1186. [CrossRef]
20. Yoo, K.; Kim, B.-S.; Kim, M.-S.; Lee, J.; Jeong, J. Dissolution of Magnesium from Serpentine Mineral in Sulfuric Acid Solution. *Mater. Trans.* **2009**, *50*, 1225–1230. [CrossRef]
21. Lacinska, A.M.; Styles, M.T.; Bateman, K.; Wagner, D.; Hall, M.R.; Gowing, C.; Brown, P.D. Acid-dissolution of antigorite, chrysotile and lizardite for ex situ carbon capture and storage by mineralisation. *Chem. Geol.* **2016**, *437*, 153–169. [CrossRef]
22. Teir, S.; Kuusik, R.; Fogelholm, C.-J.; Zevenhoven, R. Production of magnesium carbonates from serpentinite for long-term storage of CO_2. *Int. J. Miner. Process.* **2007**, *85*, 1–15. [CrossRef]
23. Wang, X.; Maroto-Valer, M.M. Dissolution of serpentine using recyclable ammonium salts for CO_2 mineral carbonation. *Fuel* **2011**, *90*, 1229–1237. [CrossRef]
24. Zhu, C.; Zhao, L.; Gao, X.; Ji, J.; Chen, J. CO_2 sequestration based study of reaction kinetics of brucite. *Quat. Sci.* **2011**, *31*, 438–446. [CrossRef]
25. Krevor, S.C.M.; Lackner, K.S. Enhancing serpentine dissolution kinetics for mineral carbon dioxide sequestration. *Int. J. Greenh. Gas Control* **2011**, *5*, 1073–1080. [CrossRef]
26. Power, I.M.; Dipple, G.M.; Southam, G. Bioleaching of Ultramafic Tailings by *Acidithiobacillus* spp. for CO_2 Sequestration. *Environ. Sci. Technol.* **2010**, *44*, 456–462. [CrossRef] [PubMed]
27. Li, Z.; Xu, J.; Teng, H.H.; Liu, L.; Chen, J.; Chen, Y.; Zhao, L.; Ji, J. Bioleaching of Lizardite by Magnesium- and Nickel-Resistant Fungal Isolate from Serpentinite Soils—Implication for Carbon Capture and Storage. *Geomicrobiol. J.* **2015**, *32*, 181–192. [CrossRef]
28. Chen, P.-C.; Kou, K.L.; Tai, H.K.; Jin, S.L.; Lye, C.L.; Lin, C.Y. Removal of carbon dioxide by reactive crystallization in a scrubber—Kinetics of barium carbonate crystals. *J. Cryst. Growth* **2002**, *237*, 2166–2171. [CrossRef]
29. Chen, P.-C.; Chen, C.; Fun, M.; Liao, O.Y.; Jiang, J.; Wang, Y.; Chen, C. Mixing and Crystallization Kinetics in Gas-liquid Reactive Crystallization. *Chem. Eng. Technol.* **2004**, *27*, 519–528. [CrossRef]
30. Chen, P.-C.; Shi, W.; Du, R.; Chen, V. Scrubbing of CO_2 Greenhouse Gases, Accompanied by Precipitation in a Continuous Bubble-Column Scrubber. *Ind. Eng. Chem. Res.* **2008**, *47*, 6336–6343. [CrossRef]
31. Kotaki, Y.; Tsuge, H. Reactive crystallization of calcium carbonate by gas-liquid and liquid-liquid reactions. *Can. J. Chem. Eng.* **1990**, *68*, 435–442. [CrossRef]
32. Tamura, K.; Tsuge, H. Characteristics of multistage column crystallizer for gas–liquid reactive crystallization of calcium carbonate. *Chem. Eng. Sci.* **2006**, *61*, 5818–5826. [CrossRef]

33. Ferrini, V.; De Vito, C.; Mignardi, S. Synthesis of nesquehonite by reaction of gaseous CO_2 with Mg chloride solution: Its potential role in the sequestration of carbon dioxide. *J. Hazard. Mater.* **2009**, *168*, 832–837. [CrossRef] [PubMed]
34. Harrison, A.L.; Power, I.M.; Dipple, G.M. Accelerated Carbonation of Brucite in Mine Tailings for Carbon Sequestration. *Environ. Sci. Technol.* **2013**, *47*, 126–134. [CrossRef] [PubMed]
35. Han, B.; Qu, H.; Niemi, H.; Sha, Z.; Louhi-Kultanen, M. Mass Transfer and Kinetics Study of Heterogeneous Semi-Batch Precipitation of Magnesium Carbonate. *Chem. Eng. Technol.* **2014**, *37*, 1363–1368. [CrossRef]
36. Hopkinson, L.; Rutt, K.; Cressey, G. The transformation of nesquehonite to hydromagnesite in the system $CaO\text{-}MgO\text{-}H_2O\text{-}CO_2$: An experimental spectroscopic study. *J. Geol.* **2008**, *116*, 387–400. [CrossRef]
37. Ballirano, P.; De Vito, C.; Mignardi, S.; Ferrini, V. Phase transitions in the $Mg\text{-}CO_2\text{-}H_2O$ system and the thermal decomposition of dypingite, $Mg_5(CO_3)_4(OH)_2{\cdot}5H_2O$: Implications for geosequestration of carbon dioxide. *Chem. Geol.* **2013**, *340*, 59–67. [CrossRef]
38. Kristova, P.; Hopkinson, L.J.; Rutt, K.J.; Hunter, H.M.A.; Cressey, G. Carbonate mineral paragenesis and reaction kinetics in the system $MgO\text{-}CaO\text{-}CO_2\text{-}H_2O$ in presence of chloride or nitrate ions at near surface ambient temperatures. *Appl. Geochem.* **2014**, *50*, 16–24. [CrossRef]
39. Derks, P.W.J.; Versteeg, G.F. Kinetics of absorption of carbon dioxide in aqueous ammonia solutions. *Energy Procedia* **2009**, *1*, 1139–1146. [CrossRef]
40. Darde, V.; Van Well, W.J.M.; Fosboel, P.L.; Stenby, E.H.; Thomsen, K. Experimental measurement and modeling of the rate of absorption of carbon dioxide by aqueous ammonia. *Int. J. Greenh. Gas Control* **2011**, *5*, 1149–1162. [CrossRef]
41. Zeng, Q.; Guo, Y.; Niu, Z.; Lin, W. The absorption rate of CO_2 by aqueous ammonia in a packed column. *Fuel Process. Technol.* **2013**, *108*, 76–81. [CrossRef]
42. Pinsent, B.R.W.; Pearson, L.; Roughton, F.J.W. The kinetics of combination of carbon dioxide with hydroxide ions. *Trans. Faraday Soc.* **1956**, *52*, 1512–1520. [CrossRef]
43. Hänchen, M.; Prigiobbe, V.; Baciocchi, R.; Mazzotti, M. Precipitation in the Mg-carbonate system—Effects of temperature and CO_2 pressure. *Chem. Eng. Sci.* **2008**, *63*, 1012–1028. [CrossRef]
44. Montes-Hernandez, G.; Renard, F.; Chiriac, R.; Findling, N.; Toche, F. Rapid Precipitation of Magnesite Microcrystals from $Mg(OH)_2\text{-}H_2O\text{-}CO_2$ Slurry Enhanced by NaOH and a Heat-Aging Step (from ∼20 to 90 °C). *Cryst. Growth Des.* **2012**, *12*, 5233–5240. [CrossRef]
45. Swanson, E.J.; Fricker, K.J.; Sun, M.; Park, A.-H.A. Directed precipitation of hydrated and anhydrous magnesium carbonates for carbon storage. *Phys. Chem. Chem. Phys.* **2014**, *16*, 23440–23450. [CrossRef] [PubMed]
46. Sayles, F.L.; Fyfe, W.S. The crystallization of magnesite from aqueous solution. *Geochim. Cosmochim. Acta* **1973**, *37*, 87–99. [CrossRef]
47. Königsberger, E.; Königsberger, L.-C.; Gamsjäger, H. Low-temperature thermodynamic model for the system $Na_2CO_3\text{-}MgCO_3\text{-}CaCO_3\text{-}H_2O$. *Geochim. Cosmochim. Acta* **1999**, *63*, 3105–3119. [CrossRef]
48. Braithwaite, C.J.R.; Zedef, V. Living hydromagnesite stromatolites from Turkey. *Sediment. Geol.* **1994**, *92*, 1–5. [CrossRef]
49. Schroll, E. Genesis of magnesite deposits in the view of isotope geochemistry. *Bol. Parana. Geocienc.* **2002**, *50*, 59–68. [CrossRef]
50. Parente, C.V.; Ronchi, L.H.; Sial, A.N.; Guillou, J.J.; Arthaud, M.H.; Fuzikawa, K.; Veríssimo, C.U.V. Geology and geochemistry of paleoproterozoic magnesite deposits (∼1.8Ga), State of Ceará, Northeastern Brazil. *Carbonates Evaporites* **2004**, *19*, 28–50. [CrossRef]
51. Jull, A.J.T.; Cheng, S.; Gooding, J.L.; Velbel, M.A. Rapid growth of magnesium-carbonate weathering products in a stony meteorite from antarctica. *Science* **1988**, *242*, 417–419. [CrossRef] [PubMed]
52. Power, I.M.; Wilson, S.A.; Thom, J.M.; Dipple, G.M.; Southam, G. Biologically induced mineralization of dypingite by cyanobacteria from an alkaline wetland near Atlin, British Columbia, Canada. *Geochem. Trans.* **2007**, *8*, 13. [CrossRef] [PubMed]
53. Fischbeck, R.; Müller, G. Monohydrocalcite, hydromagnesite, nesquehonite, dolomite, aragonite, and calcite in speleothems of the Fränkische Schweiz, Western Germany. *Contrib. Mineral. Petrol.* **1971**, *33*, 87–92. [CrossRef]

54. Davies, P.J.; Bubela, B. *The Transformation of Nesquehonite to Hydromagnesite*; Bureau of Mineral Resources, Geology and Geophysics; Bureau of Mineral Resources and Baas, Becking Geobiological Laboratory, Division of Mineralogy: Canberra, Australia, 1973; p. 31.
55. Hopkinson, L.; Kristova, P.; Rutt, K.; Cressey, G. Phase transitions in the system MgO–CO_2–H_2O during CO_2 degassing of Mg-bearing solutions. *Geochim. Cosmochim. Acta* **2012**, *76*, 1–13. [CrossRef]
56. Zhang, Z.; Zheng, Y.; Ni, Y.; Liu, Z.; Chen, J.; Liang, X. Temperature- and pH-Dependent Morphology and FT−IR Analysis of Magnesium Carbonate Hydrates. *J. Phys. Chem. B* **2006**, *110*, 12969–12973. [CrossRef] [PubMed]
57. Zhu, C.; Yao, X.; Zhao, L.; Teng, H.H. A composite reactor with wetted-wall column for mineral carbonation study in three-phase systems. *Rev. Sci. Instrum.* **2016**, *87*, 115115. [CrossRef] [PubMed]
58. Zhao, L.; Zhu, C.; Ji, J.; Chen, J.; Teng, H.H. Thermodynamic and kinetic effect of organic solvent on the nucleation of nesquehonite. *Geochim. Cosmochim. Acta* **2013**, *106*, 192–202. [CrossRef]
59. Zhu, C.; Wang, Z.; Zhao, L. The effect of solution chemistry on nucleation of nesquehonite. *Am. J. Sci.* **2016**, *316*, 1027–1053. [CrossRef]
60. Schulz, K.G.; Riebesell, U.; Rost, B.; Thoms, S.; Zeebe, R.E. Determination of the rate constants for the carbon dioxide to bicarbonate inter-conversion in pH-buffered seawater systems. *Mar. Chem.* **2006**, *100*, 53–65. [CrossRef]
61. Mani, F.; Peruzzini, M.; Stoppioni, P. CO_2 absorption by aqueous NH_3 solutions: Speciation of ammonium carbamate, bicarbonate and carbonate by a ^{13}C NMR study. *Green Chem.* **2006**, *8*, 995. [CrossRef]
62. Wang, X.; Conway, W.; Fernandes, D.; Lawrance, G.; Burns, R.; Puxty, G.; Maeder, M. Kinetics of the Reversible Reaction of $CO_2(aq)$ with Ammonia in Aqueous Solution. *J. Phys. Chem. A* **2011**, *115*, 6405–6412. [CrossRef] [PubMed]
63. Clegg, S.L.; Whitfield, M. A chemical model of seawater including dissolved ammonia and the stoichiometric dissociation constant of ammonia in estuarine water and seawater from −2 to 40 °C. *Geochim. Cosmochim. Acta* **1995**, *59*, 2403–2421. [CrossRef]
64. Earnshaw, A.; Greenwood, N. *Chemistry of the Elements, Second Edition*, 2nd ed.; Butterworth-Heinemann: Oxford, UK, 1997; ISBN 0-7506-3365-4.
65. Hostetler, P.B. The degree of saturation of magnesium and calcium carbonate minerals in natural waters. *Int. Assoc. Sci. Hydrol. Commun. Subterr. Waters Publ.* **1964**, *64*, 34–49.
66. Marion, G.M. Carbonate mineral solubility at low temperatures in the Na-K-Mg-Ca-H-Cl-SO_4-OH-HCO_3-CO_3-CO_2-H_2O system. *Geochim. Cosmochim. Acta* **2001**, *65*, 1883–1896. [CrossRef]
67. Blake, S.; Cuff, C. Preparation and Use of Cationic Halides, Sequestration of Carbon Dioxide 2007. Patent WO2007003013A1, 11 January 2007.
68. Cheng, W.; Li, Z. Nucleation kinetics of nesquehonite ($MgCO_3 \cdot 3H_2O$) in the $MgCl_2-Na_2CO_3$ system. *J. Cryst. Growth* **2010**, *312*, 1563–1571. [CrossRef]
69. Wang, D.; Li, Z. Gas–Liquid Reactive Crystallization Kinetics of Hydromagnesite in the $MgCl_2$-CO_2-NH_3-H_2O System: Its Potential in CO_2 Sequestration. *Ind. Eng. Chem. Res.* **2012**, *51*, 16299–16310. [CrossRef]
70. Haynes, W.M. *CRC Handbook of Chemistry and Physics*, 95th ed.; CRC press: Boca Raton, FL, USA, 2014.
71. DeCoursey, W.J. Absorption with chemical reaction: Development of a new relation for the Danckwerts model. *Chem. Eng. Sci.* **1974**, *29*, 1867–1872. [CrossRef]
72. Pinsent, B.R.W.; Pearson, L.; Roughton, F.J.W. The kinetics of combination of carbon dioxide with ammonia. *Trans. Faraday Soc.* **1956**, *52*, 1594–1598. [CrossRef]
73. Qin, F.; Wang, S.; Hartono, A.; Svendsen, H.F.; Chen, C. Kinetics of CO_2 absorption in aqueous ammonia solution. *Int. J. Greenh. Gas Control* **2010**, *4*, 729–738. [CrossRef]
74. Crooks, J.E.; Donnellan, J.P. Kinetics and mechanism of the reaction between carbon dioxide and amines in aqueous solution. *J. Chem. Soc. Perkin Trans. 2* **1989**, *0*, 331–333. [CrossRef]
75. Liu, J.; Wang, S.; Zhao, B.; Tong, H.; Chen, C. Absorption of carbon dioxide in aqueous ammonia. *Energy Procedia* **2009**, *1*, 933–940. [CrossRef]
76. Zhao, L.; Sang, L.; Chen, J.; Ji, J.; Teng, H.H. Aqueous Carbonation of Natural Brucite: Relevance to CO_2 Sequestration. *Environ. Sci. Technol.* **2010**, *44*, 406–411. [CrossRef] [PubMed]
77. Highfield, J.; Lim, H.; Fagerlund, J.; Zevenhoven, R. Mechanochemical processing of serpentine with ammonium salts under ambient conditions for CO_2 mineralization. *RSC Adv.* **2012**, *2*, 6542–6548. [CrossRef]

78. Dell, R.M.; Weller, S.W. The thermal decomposition of nesquehonite $MgCO_3 \cdot 3H_2O$ and magnesium ammonium carbonate $MgCO_3 \cdot (NH_4)_2CO_3 \cdot 4H_2O$. *Trans. Faraday Soc.* **1959**, *55*, 2203–2220. [CrossRef]
79. Power, I.M.; Harrison, A.L.; Dipple, G.M. Accelerating Mineral Carbonation Using Carbonic Anhydrase. *Environ. Sci. Technol.* **2016**, *50*, 2610–2618. [CrossRef] [PubMed]
80. Levenspiel, O. *Chemical Reaction Engineering*, 3rd ed.; Wiley: New York, NY, USA, 1999; ISBN 0-471-25424-X.
81. Hollingbery, L.A.; Hull, T.R. The fire retardant behaviour of huntite and hydromagnesite—A review. *Polym. Degrad. Stab.* **2010**, *95*, 2213–2225. [CrossRef]
82. Hollingbery, L.A.; Hull, T.R. The fire retardant effects of huntite in natural mixtures with hydromagnesite. *Polym. Degrad. Stab.* **2012**, *97*, 504–512. [CrossRef]
83. Hull, T.R.; Witkowski, A.; Hollingbery, L. Fire retardant action of mineral fillers. *Polym. Degrad. Stab.* **2011**, *96*, 1462–1469. [CrossRef]
84. Glasser, F.P.; Jauffret, G.; Morrison, J.; Galvez-Martos, J.-L.; Patterson, N.; Imbabi, M.S.-E. Sequestering CO_2 by Mineralization into Useful Nesquehonite-Based Products. *Front. Energy Res.* **2016**, *4*. [CrossRef]
85. Walling, S.A.; Provis, J.L. Magnesia-Based Cements: A Journey of 150 Years, and Cements for the Future? *Chem. Rev.* **2016**, *116*, 4170–4204. [CrossRef] [PubMed]
86. Jones, B.F.; Deocampo, D.M. Geochemistry of Saline Lakes. In *Treatise on Geochemistry*; Elsevier: Amsterdam, The Netherlands, 2003; pp. 393–424. ISBN 978-0-08-043751-4.
87. Zhang, B. Development and Countermeasures of Magnesium Salt Industry in Salt Lakes of Qaidam Basin. *Sea Lake Salt Chem. Ind.* **2001**, 17–21. [CrossRef]